

The propagation of statistical errors in covariant density functional theory: ground state observables and single-particle properties.

S. E. Agbemava,¹ A. V. Afanasjev,¹ and A. Taninah¹

¹*Department of Physics and Astronomy, Mississippi State University, MS 39762*

(Dated: November 29, 2018)

Statistical errors in ground state observables and single-particle properties of spherical even-even nuclei and their propagation to the limits of nuclear landscape have been investigated in covariant density functional theory (CDFT) for the first time. In this study we consider only covariant energy density functionals with non-linear density dependency. Statistical errors for binding energies and neutron skins significantly increase on approaching two-neutron drip line. On the contrary, such a trend does not exist for statistical errors in charge radii and two-neutron separation energies. The absolute and relative energies of the single-particle states in the vicinity of the Fermi level are characterized by low statistical errors ($\sigma(e_i) \sim 0.1$ MeV). Statistical errors in the predictions of spin-orbit splittings are rather small. Statistical errors in physical observables are substantially smaller than related systematic uncertainties. Thus, at the present level of the development of theory, theoretical uncertainties at nuclear limits are dominated by systematic ones. Statistical errors in the description of physical observables related to the ground state and single-particle degrees of freedom are typically substantially lower in CDFT as compared with Skyrme density functional theory. The correlations between the model parameters are studied in detail. The parametric correlations are especially pronounced for the g_2 and g_3 parameters which are responsible for the density dependence of the model. The accounting of this fact potentially allows to reduce the number of free parameters of non-linear meson coupling model from six to five.

PACS numbers: 21.10.Dr, 21.10.Pc, 21.10.Ft, 21.60.Jz, 21.60.Ka

I. INTRODUCTION

Although significant progress has been achieved over the years in the development of theoretical tools for the description of low-energy nuclear phenomena, some simplifications and approximations are still necessary because of the complexity of nuclear many-body problem and the impossibility of its exact solution for the systems with large number of particles. In addition, fine details of nuclear force and its dependence on density are still not fully resolved. As a result, it becomes necessary to estimate theoretical uncertainties in the description of physical observables [1–3]. This is especially important when one deals with the extrapolations beyond the known regions, as, for example, in particle number or deformation, since experimental data which acts as a substitute of exact solution are not available there. Such estimates are also required for the evaluation of predictive power of the models and the robustness of their predictions. The need for such estimates has been clearly recognized by nuclear theory community as illustrated by a substantial number of the studies aiming at the quantification of theoretical uncertainties in nuclear structure, nuclear reactions and nuclear astrophysics (see Refs. [3–10] and references quoted therein).

There are two types of theoretical uncertainties: systematic and statistical ones [2, 11]. *Systematic* theoretical uncertainties emerge from underlying theoretical approximations. In the framework of density functional theory (DFT), there are two major sources of these approximations, namely, the range of interaction and the form of the density dependence of the effective interac-

tion [12, 13]. In the non-relativistic case one has zero range Skyrme and finite range Gogny forces and different density dependencies [12, 14]. A similar situation exists also in the relativistic case: point coupling and meson exchange models have an interaction of zero and of finite range, respectively [15–18]. The density dependence is introduced either through an explicit dependence of the coupling constants [16, 18, 19] or via non-linear meson couplings [13, 17]. This ambiguity in the definition of the range of the interaction and its density dependence leads to several major classes of the covariant energy density functionals (CEDF) which were discussed in Ref. [3].

It is necessary to recognize that precise quantification of *systematic errors* in the regions of nuclear chart for which experimental data is not available is not possible due to a number of reasons [2, 3]. Thus, we prefer to use the notation *systematic uncertainties* (instead of *systematic errors* introduced in Ref. [2]) which has more narrow meaning since they are defined with respect of selected set of the functionals (see introduction of Ref. [3]).

An additional source of theoretical uncertainties is related to the details of the fitting protocol such as the choice of experimental data and the selection of adopted errors. It applies only to a given functional and the related theoretical uncertainties are called *statistical errors* [2, 11]. Note that the selection of adopted errors is to a degree subjective, in particular, if one deals with quantities of different dimensions.

The covariant density functional theory (CDFT) represents a relativistic extension of the DFT framework to the nuclear many-body problem [15]. It exploits basic properties of QCD at low energies, in particular symmetries

and the separation of scales [20]. It provides a consistent treatment of the spin degrees of freedom and spin-orbit splittings [21] and includes the complicated interplay between the large Lorentz scalar and vector self-energies induced on the QCD level by the in-medium changes of the scalar and vector quark condensates [22]. In addition, CEDFs include *nuclear magnetism* [23], i.e. a consistent description of currents and time-odd mean fields [24], for which no new adjustable parameters are required because of Lorentz invariance. The CDFT has been successfully applied to the description of a large variety of nuclear phenomena (see reviews in Refs. [15, 25–27]).

However, only recently systematic efforts have been undertaken to quantify theoretical uncertainties in the description of physical observables within the CDFT framework. Systematic uncertainties, their sources and their propagation to the extremes of neutron number have been studied globally for the ground state masses, deformations, two-particle separation energies, charge radii and neutrons skins of even-even nuclei, as well as for the positions of drip lines in Refs. [3, 5, 28–31]. In Ref. [29] systematic uncertainties in the predictions of the ground state properties of superheavy nuclei have been investigated. Above mentioned investigations were restricted to even-even nuclei which are either spherical or have only even-multipole deformations in the ground state. This restriction has been removed in Refs. [30, 32] in which the global studies of octupole deformed nuclei and related systematic uncertainties in their description have been performed. The investigations of systematic uncertainties have also been carried out for excited states such as inner fission barriers in superheavy nuclei (Ref. [33]), deformed one-quasiparticle states in odd-mass actinides [34, 35] and rotational states in even-even and odd-mass actinides (Ref. [36]).

Although impressive amount of data on systematic uncertainties in the description of physical observables in the CDFT has been collected within last few years, very little is known about related statistical errors. So far, they have been investigated only for potential energy curves in a single superheavy nucleus for two CEDFs in Ref. [33]. To fill this gap in our knowledge of the performance of CEDFs, the present manuscript aims on a systematic study of statistical errors in the description of the ground state and single-particle properties of spherical nuclei.

A second goal of the present investigation is to establish the correlations between the CEDF parameters and to see whether these parameters are independent. Such correlations have not been studied systematically so far in the CDFT framework. Their presence affects statistical errors in the description of physical observables [37]. The removal of parametric correlations leads to the reduction of the dimensionality of the parameter hyperspace and to the decrease of statistical errors. The latter was illustrated in Ref. [37] on the example of the study of statistical errors in the single-particle energies of spherical nuclei performed with Woods-Saxon potential.

So far, mostly the covariance analysis has been used in the studies of statistical errors for physical observables in the DFT framework (see, for example, Refs. [2, 6, 38, 39]). However, in the calculations of the covariance matrix a linearized least-square system in the vicinity of the minimum of objective function χ_{norm}^2 is usually assumed [11]. This means that the covariance analysis assumes that full information about statistical errors is contained in the derivatives taken at the optimum parametrization and ignores potential non-linear dependence of the observables on the coupling constants in the parts of the parameter hyperspace away from the optimum parametrization. However, there is no guarantee that linear approximation is valid for non-linear problems in the region of the parameter hyperspace away from the optimum parametrization (see Ref. [11]). If that is a case the covariance matrix loses its validity [11]. A priori such non-linearities, which are present in the CDFT models, cannot be disregarded. For example, the analysis of the correlations between the α_S and α_V parameters in point coupling models performed in Ref. [40] clearly indicates their presence.

Thus, we use alternative approach based on the Monte-Carlo method in which randomly generated functionals are accepted/rejected based on the condition of Eq. (4) given in Sec. II below. As a result, the set of reasonable functionals is generated which is used for the calculations of statistical errors in the physical observables of interest (see Sec. II). The advantage of this method is that its outcome is defined by full parameter hyperspace used in the analysis (and not only by the neighborhood of optimum parametrization as in covariance analysis). This allows to take existing non-linearities between the parameters fully into account. Thus, the Monte-Carlo approach is free from above mentioned deficiencies of the covariance analysis. However, it is much more numerically time consuming than relatively simple covariance analysis and requires significant computational power. As a result, so far it was applied only to the analysis of statistical errors in the single-particle energies of phenomenological Woods-Saxon potential (see Ref. [37]). Because of this reason we focus in the present exploratory study on the non-linear (NL) CEDFs which are characterized by the minimum number of the parameters (and, as a consequence, by minimal dimensionality of the parameter hyperspace) among the state-of-the-art CEDFs. Their six parameters are the mass m_σ and coupling constant g_σ of the σ -meson, the coupling constant g_ω of the ω -meson, the coupling constant g_ρ of the ρ meson which is responsible for the isovector channel of the functional and the coupling constants g_2 and g_3 which define the density dependence of the functional.

The paper is organized as follows. Section II describes the details of the analysis of statistical errors. Fitting protocols and related theoretical uncertainties are discussed in Sec. III. The ranges of the parameters and parametric correlations in the functionals are discussed in Sec. IV. Statistical errors in the description of the ground

state observables of spherical even-even nuclei and their propagation towards neutron drip line are investigated in Sec. V. Sec. VI is devoted to the discussion of statistical errors in the description of single-particle energies and their consequences for the predictions at the extremes of neutron number and charge. Note that statistical errors discussed in Secs. V and VI are compared with available systematic uncertainties estimated previously in Refs. [3, 5, 29, 31]. Finally, Sec. VII summarizes the results of our work.

II. STATISTICAL ERRORS AND THE DETAILS OF THE CALCULATIONS

The normalized objective function is defined for model having N_{par} adjustable parameters $\mathbf{p} = (p_1, p_2, \dots, p_{N_{par}})$ as

$$\chi_{norm}^2(\mathbf{p}) = \frac{1}{s} \sum_{i=1}^{N_{type}} \sum_{j=1}^{n_i} \left(\frac{O_{i,j}(\mathbf{p}) - O_{i,j}^{exp}}{\Delta O_{i,j}} \right)^2 \quad (1)$$

where

$$s = \frac{\chi^2(\mathbf{p}_0)}{N_{data} - N_{par}} \quad (2)$$

is global scale factor (Birge factor [41]) defined at the minimum of the penalty function (optimum parametrization \mathbf{p}_0 ¹) which leads to the average $\chi^2(\mathbf{p}_0)$ per degree of freedom equal to one [2] and

$$N_{data} = \sum_{i=1}^{N_{type}} n_i \quad (3)$$

is the total number of data points of different types. Here, N_{type} stands for the number of different data types. The calculated and experimental/empirical values of physical observable j of the i -th type are represented by $O_{i,j}(\mathbf{p})$ and $O_{i,j}^{exp}$, respectively. $\Delta O_{i,j}$ is adopted error for physical observable $O_{i,j}$. These quantities for the functionals under study are summarized in Table I.

The acceptable functionals are defined from the condition [2]

$$\chi_{norm}^2(\mathbf{p}) \leq \chi_{norm}^2(\mathbf{p}_0) + 1. \quad (4)$$

This condition specifies the 'physically reasonable' domain around \mathbf{p}_0 in which the parametrization \mathbf{p} provides a reasonable fit and thus can be considered as acceptable. This domain is the N -dimensional parameter hyperspace $\mathbf{P}_{space} = [p_{1_{min}} - p_{1_{max}}, p_{2_{min}} - p_{2_{max}}, \dots, p_{N_{min}} - p_{N_{max}}]$, where $p_{i_{min}}$ and $p_{i_{max}}$ represent the lower and upper boundaries for the variation of the i -th parameter.

These boundaries are defined in such a way that their further increase (for $p_{i_{max}}$) or decrease (for $p_{i_{min}}$) does not lead to additional points in parameter hyperspace which satisfy Eq. (4).

The numerical calculations are performed in the following way. New parametrizations \mathbf{p} are randomly generated in the N -dimensional parameter hyperspace and they are accepted if the condition (4) is satisfied. Using the set $[\mathbf{p}_1, \mathbf{p}_2, \dots, \mathbf{p}_M]$ of M accepted functional variations the calculations are performed for spherical nuclei in the Ca, Ni, Sn and Pb isotope chains from proton to neutron drip lines. For each nucleus the mean values of physical observables

$$\bar{O}_{i,j} = \frac{1}{M} \sum_{k=1}^M O_{i,j}(\mathbf{p}_k) \quad (5)$$

and their standard deviations

$$\sigma_{i,j} = \sqrt{\frac{1}{M} \sum_{k=1}^M [O_{i,j}(\mathbf{p}_k) - \bar{O}_{i,j}]^2} \quad (6)$$

are calculated. The latter serves as a measure of statistical error.

As mentioned in the introduction we consider here only non-linear meson coupling models which are characterized by the minimal set of the parameters amongst different classes of the CDFT models. In the meson-exchange models [17, 42], the nucleus is described as a system of Dirac nucleons interacting via the exchange of mesons with finite masses leading to finite-range interactions. The starting point is a standard Lagrangian density [43]

$$\begin{aligned} \mathcal{L} = & \bar{\psi} [\gamma \cdot (i\partial - g_\omega \omega - g_\rho \vec{\rho} \vec{\tau} - eA) - m - g_\sigma \sigma] \psi \\ & + \frac{1}{2}(\partial\sigma)^2 - U(\sigma) - \frac{1}{4}\Omega_{\mu\nu}\Omega^{\mu\nu} + \frac{1}{2}m_\omega^2\omega^2 \\ & - \frac{1}{4}\vec{R}_{\mu\nu}\vec{R}^{\mu\nu} + \frac{1}{2}m_\rho^2\rho^2 - \frac{1}{4}F_{\mu\nu}F^{\mu\nu} \end{aligned} \quad (7)$$

which contains nucleons described by the Dirac spinors ψ with the mass m and several effective mesons characterized by the quantum numbers of spin, parity, and isospin. They create effective fields in a Dirac equation, which corresponds to the Kohn-Sham equation [44] of non-relativistic density functional theory. The density dependence is introduced into model via a non-linear meson coupling [13]

$$U(\sigma) = \frac{1}{2}m_\sigma^2\sigma^2 + \frac{1}{3}g_2\sigma^3 + \frac{1}{4}g_3\sigma^4. \quad (8)$$

In simplest ansatz, the Lagrangian (7) contains as parameters the mass m_σ of the σ meson, the coupling constants g_σ , g_ω , and g_ρ as well as density dependent parameters g_2 and g_3 . The masses m , m_ω and m_ρ are typically fixed in non-linear meson coupling models. e is the charge of the protons and it vanishes for neutrons.

The calculations have been performed using the spherical RHB code. The truncation of the basis is performed

¹ Because of the experimental errors and incompleteness of the physical modelling optimum parametrizations of the models are known only up to their uncertainty probability distributions [37].

in such a way that all states belonging to the shells up to $N_F = 20$ fermionic shells and $N_B = 20$ bosonic shells are taken into account. In order to avoid the uncertainties connected with the definition of the size of the pairing window we use the separable form of the finite range Gogny pairing interaction introduced by Tian et al [45] with the strength of pairing defined in Ref. [3]. This is also done for the consistency with previous global studies of systematic uncertainties in the description of physical observables within the CDFT framework [3, 5, 28–31].

III. FITTING PROTOCOLS: AN EXAMPLE OF THE ORIGIN OF THE UNCERTAINTIES

Previous fits of the non-linear CEDFs have been performed in the RMF+BCS framework with simple pairing (see Refs. [17, 46–49] for details). Since in the present work the RHB framework with separable pairing of finite range is used in fitting protocol for the first time, the investigation of the dependence of the optimum parametrization on the details of the fitting protocol is performed.

The starting point is the fitting protocol of the NL3* functional (see Ref. [17]). The types of the input data for this protocol and related adopted errors are summarized in column 2 of Table I. The minimization within this protocol leads to optimum functional labeled NL5(A) (see Table II). When considering the quality of the functional we take into account the ranges of the nuclear matter properties recommended for relativistic functionals in Ref. [50]. These are $\rho_0 \sim 0.15 \text{ fm}^{-3}$, $E/A \sim -16 \text{ MeV}$, $K_0 = 190 - 270$, $J = 25 - 35 \text{ MeV}$ ($J = 20 - 35 \text{ MeV}$) and $L_0 = 25 - 115$ ($L_0 = 30 - 80$) for the SET2a (SET2b) sets of the constraints on the experimental/empirical ranges for the quantities of interest. As compared with the CEDF NL3*, the NL5(A) functional has better J and L_0 values but much worse K_0 value. The analysis of the contributions of physical observables of different classes shows that χ_{total}^2 is dominated by the contributions from 4 data points on neutron skins with the contribution of the single data point on the neutron skin of ^{90}Zr providing 22.1% of χ_{total}^2 . These large contributions from neutron skin data to χ_{total}^2 clearly illustrate that these functionals cannot accurately describe presently adopted experimental values of r_{skin} obtained by means of hadronic probes².

To compensate for too large value of K_0 and to force it to more acceptable value, the adopted error for K_0 has been reduced from 10% to 2.5% in the fitting protocol of the NL5(B) functional (see column 3 of Table I). This functional and related nuclear matter properties as well as penalty function contributions are shown in Table II. Its E/A , ρ_0 and K_0 values are close to the NL3* ones, but it has better symmetry energy J and the slope of symmetry energy L_0 . However, similar to NL5(A) it suffers from too large contribution of neutron skins (and especially, the one coming from ^{90}Zr) to χ_{total}^2 .

To reduce this problem, the neutron skin of ^{90}Zr has been dropped from the fitting protocol of the NL5(C) functional³ (see column 4 in Table I.) This functional has E/A , ρ_0 and K_0 values similar to the ones of the NL3* and NL5(B) functionals (see Table II). Its J and L_0 values are better than those of the NL3* functional but slightly worse as compared with those of the NL5(B) one. However, the NL5(C) functional provides better description of binding energies and charge radii as compared with the NL5(A) and NL5(B) ones; these are physical observables which are precisely measured in experiment. On the other hand, it gives slightly worse description of neutron skins in the ^{116}Sn , ^{124}Sn and ^{208}Pb nuclei but as mentioned before this physical observable is characterized by substantial experimental uncertainties.

One can consider removing the neutron skins (as least reliable experimental data on finite nuclei) from the fitting protocol; this leads to the NL5(D) functional (see Table II). It is characterized by a substantial reduction (by a factor of 2 as compared with the CEDF NL5(C)) of the error in the reproduction of experimental data on binding energies. However, for this functional the J and L_0 values deviate more from recommended values as compared with the NL5(C) one.

Alternatively, one can use experimental errors (from Refs. [53–55]) as adopted errors for neutron skins which are substantially larger than adopted errors (5%) of the fitting protocol of the NL5(A-C) functionals (Table I). This leads to the NL5(E) functional in which the impact of neutron skins on total χ_{total}^2 is substantially reduced as compared with NL5(A-C) functionals. As a consequence, the nuclear matter properties of the NL5(D) and NL5(E) functionals are similar and they provide comparable description of binding energies and charge radii.

The results presented here clearly show that the selection of the fitting protocol (physical observables and re-

² There is a significant controversy in the adopted experimental values of neutron skins (see discussion in Sect. [3] and in Ref. [51]). For example, the experiments based on hadronic probes provide neutron skin in ^{208}Pb around 0.2 fm or slightly smaller. However, these experimental data are extracted in model-dependent ways. Alternatively, a measurement using an electroweak probe has been carried out in parity violating electron scattering on nuclei (PREX) and it brings $r_{skin} = 0.33 \pm 0.17$ [51]. A central value of 0.33 fm is particularly in-

triguing because it is around 0.13 fm higher than central values obtained in other experiments. The electroweak probe has the advantage over experiments using hadronic probes that it allows a nearly model-independent extraction of the neutron radius that is independent of most strong interaction uncertainties [52]. Note that non-linear CEDFs typically give $r_{skin} \sim 0.3$ fm, so if the central value $r_{skin} \sim 0.33$ obtained in PREX experiment would be confirmed in future PREX-2 experiment [52], this would lead to substantial reduction of χ_{skin}^2 .

³ The same procedure has been employed in the fitting protocol of the DD-ME2 functional in Ref. [16].

TABLE I. Input data for fitting protocol of the NL5() CEDFs. The number n_i of experimental (empirical) data points and adopted errors $\Delta O_{i,j}$ are presented for each type of data. The binding energies of the ^{16}O , ^{40}Ca , ^{48}Ca , ^{72}Ni , ^{90}Zr , ^{116}Sn , ^{124}Sn , ^{132}Sn , ^{204}Pb , ^{208}Pb , ^{214}Pb and ^{210}Po nuclei, the charge radii of ^{16}O , ^{40}Ca , ^{48}Ca , ^{90}Zr , ^{116}Sn , ^{124}Sn , ^{204}Pb , ^{208}Pb and ^{214}Pb nuclei as well as neutron skins of the ^{90}Zr , ^{116}Sn , ^{124}Sn and ^{208}Pb nuclei are used in the fitting protocol. In addition, employed empirical values $O_{i,j}$ for the properties of symmetric nuclear matter at saturation are provided; these are the density ρ_0 , the energy per particle E/A , the incompressibility K_0 and the symmetry energy J . The columns 3-6 show only the changes with respect of the values provided in column 2.

	NL5(A)	NL5(B)	NL5(C)	NL5(D)	NL5(E)
1	2	3	4	5	6
1. Masses E (MeV)					
n_1	12				
ΔE [MeV]	$0.001E$				
2. Charge radii r_{ch} (fm)					
n_2	9				
Δr_{ch} [fm]	$0.002 r_{ch}$				
3. Neutron skin r_{skin} (fm)					
n_3	4		3 [no ^{90}Zr]	0	
Δr_{skin} [fm]	$0.05 r_{skin}$				see text
4. Nuclear matter properties					
n_4	4				
E/A [MeV]	-16.0				
$\Delta E/A$ [MeV]	$0.05E/A$				
ρ [fm^{-3}]	0.153				
$\Delta\rho$ [fm^{-3}]	0.1ρ				
K_0 [MeV]	250.0				
ΔK_0 [MeV]	$0.1K_0$	$0.025K_0$	$0.025K_0$	$0.025K_0$	$0.025K_0$
J [MeV]	33.0				
ΔJ [MeV]	$0.1J$				
Parameters of Eq. (1)					
N_{data}	29		28	25	
N_{par}	6				
N_{type}	4			3	

lated adopted errors) is to a degree subjective. Definitely the use of more experimental data of different types is expected to reduce this level of subjectivity but it cannot be completely eliminated. Since the Monte-Carlo analysis of statistical errors is numerically extremely time-consuming, we restrict our investigation of statistical errors of non-linear CEDFs to NL5(C) and NL5(A) functionals.

IV. THE RANGES OF THE PARAMETERS AND PARAMETRIC CORRELATIONS IN THE FUNCTIONALS

In meson exchange models the general features of the nuclei are dominated by the properties of the σ and ω mesons which are responsible for intermediate range attraction and short range repulsion. They lead to attractive scalar S and repulsive vector V potentials with magnitudes of $S \approx -400$ MeV/nucleon and $V \approx +350$ MeV/nucleon [56, 57]. Their sum defines the depth of nucleonic potential (~ -50 MeV/nucleon).

Because of these large magnitudes, very small variations of the masses and coupling constants of these two mesons lead to substantial changes in binding energies

(see Figs. 1a and d). Note that in this chapter instead of functional parameters par_i we are using the ratio

$$f_i = \frac{par_i}{par_i^{opt}} \quad (9)$$

where par_i^{opt} is the value of the parameter in the optimum functional and i indicates the type of the parameter. This allows to better understand the range of the variations of the parameters and related parametric correlations in the functionals.

Coming back to Figs. 1a and d, one can see that $\pm 5\%$ change in the values of m_σ , g_σ and g_ω leads to the changes of binding energies in the range of 2000-3000 MeV. Other physical observables used in the fitting protocols such as charge radii r_{ch} also sensitively depend on f_i (see Figs. 1b and e). However, some flexibility in acceptable ranges of these parameters is provided by the fact that binding energies and charge radii have different dependencies on $f(m_\sigma)$, $f(g_\sigma)$ and $f(g_\omega)$ (see Fig. 1).

Above discussed features lead to the fact that the m_σ , g_σ and g_ω parameters are well localized in the parameter hyperspace of all meson-exchange CEDFs (see Fig. 2). Note that the absolute majority of these parameters are located within 5% deviation band with respect to mean value. This similarity between the functionals becomes

TABLE II. Different functionals obtained in the present work. The details of the fitting protocols are discussed in the text. First part of the table shows the parameters of the functionals. Note that the masses of nucleon, ω and ρ mesons are fixed at $m_N = 939.0$ MeV, $m_\omega = 782.6$ MeV and $m_\rho = 763.0$ MeV, respectively. Related nuclear matter properties are displayed in the second part of the table. In addition to those quoted in Table I, they also include the slope of the symmetry energy L_0 . Total penalty function χ_{total}^2 and the contributions to it coming from nuclear matter properties (χ_{NM}^2), binding energies (χ_E^2), charge radii (χ_{Rch}^2) and neutron skins (χ_{Nskin}^2) [and, in particular, the contribution of neutron skin of ^{90}Zr ($\chi_{Nskin(Zr)}^2$)] are presented in the last part of the table. Note that these contributions are given both in absolute values and in percentages [in parantheses] with respect of χ_{total}^2 . In addition, the penalty function per degree of freedom $\chi_{total}^2/\text{degree}$ (Birge factor) is provided. For comparison, the NL1 [46] (which is historically the first succesful CEDF) and NL3* [17] CEDFs and their nuclear matter properties are included in columns 2 and 3. The global performance of the NL3*, NL5(C), NL5(D) and NL5(E) functionals in the description of ground state properties of even-even nuclei is discussed in Appendix A.

	NL1	NL3*	NL5(A)	NL5(B)	NL5(C)	NL5(D)	NL5(E)
1. Parameters							
m_σ	492.250	502.574200	516.993054	503.253177	502.481217	503.122989	503.298890
g_σ	10.1377	10.094400	10.165747	9.896631	9.900244	10.187753	10.263955
g_ω	13.2846	12.806500	12.658290	12.457831	12.489590	12.940276	13.052487
g_ρ	4.9757	4.574800	4.277136	4.202553	4.318575	4.589814	4.582673
g_2	-12.1742	-10.809300	-8.350509	-10.925997	-10.821667	-10.858440	-10.976703
g_3	-36.2646	-30.148600	-19.260373	-28.502727	-28.27378	-30.993091	-32.006687
2. Nuclear matter properties							
E/A	-16.42	-16.31	-16.25	-16.20	-16.24	-16.29	-16.27
ρ_0	0.152	0.150	0.146	0.150	0.150	0.150	0.150
K_0	211.11	258.27	318.42	259.22	260.673	256.50	252.96
J	43.46	38.68	34.92	34.92	35.925	38.87	38.93
L_0	140.07	122.68	108.85	108.33	112.31	123.98	124.96
2. Penalty function contributions							
χ_{total}^2			343.901	367.822	273.014	74.973	85.049
$\chi_{total}^2/\text{degree}$			14.95	15.99	12.41	3.9459	3.698
χ_{NM}^2 (%)			8.120 (2.3 %)	2.626 (0.5 %)	3.842 (1.1 %)	4.434 (5.3 %)	3.625 (3.5 %)
χ_E^2 (%)			128.318 (37.3 %)	145.727 (39.6 %)	111.550 (40.9 %)	55.221 (73.7 %)	51.231 (60.2 %)
χ_{Rch}^2 (%)			34.231 (9.9 %)	18.363 (5.0 %)	16.124 (5.9 %)	15.318 (20.4 %)	16.802 (19.7 %)
χ_{Nskin}^2 (%)			173.235 (50.4 %)	201.105 (54.6 %)	141.498 (51.8 %)	0 (0.0 %)	13.390 (15.7 %)
$\chi_{Nskin(Zr)}^2$ (%)			76.071 (22.1 %)	86.591 (23.5 %)	0 (0.0 %)	0 (0.0 %)	1.178 (1.4 %)

even more striking if we consider the ratios $\frac{g_i}{m_i}$ (see Figs. 2c and f). In reality, many physical observables depend on such ratios in the CDFT framework. For example, the vector and scalar fields of the CDFT are proportional to $\left(\frac{g_\omega}{m_\omega}\right)^2$ and $\left(\frac{g_\sigma}{m_\sigma}\right)^2$ in the lowest order [56]. Another example is the equation of the state of nuclear matter which depends on the ratios $\frac{g_i}{m_i}$ [19]. Effective meson-nucleon coupling in nuclear matter is also determined by such ratios [16].

This is a unique feature of the CDFT not present in the non-relativistic DFTs. The later ones are characterized by a substantial spread of all parameters in optimum parametrizations (see discussion in Appendix B).

On the contrary, the impact of the terms which define isovector dependence, such as the ρ -meson, and density-dependent terms (such as g_2 and g_3) on total binding energies and charge radii is substantially smaller (see Fig. 1a, b, d and e). For example, to get comparable changes in binding energy of ^{208}Pb , the changes in the g_2 , g_3 and especially g_ρ parameters have to be substantially larger

than those for the m_σ , g_σ and g_ρ parameters (Table III⁴). In general, the g_ρ parameter has significantly larger impact on neutron skin than other parameters (see Fig. 1c). However, in the vicinity of the optimum functional its impact is comparable with the ones of other parameters (see Fig. 1f). Note also that the potential range of the variations of the g_ρ , g_2 and g_3 parameters is substantially larger as compared with the range of variations of the g_σ , m_σ and g_ω parameters (see Fig. 1).

Fig. 3 shows that the level of localization of the g_ρ parameter in the parameter hyperspace is lower as compared with the parameters of the σ and ω mesons. The largest deviations from the mean ρ_ρ value, defined over the set of considered functionals, are seen for the models with explicit density dependencies (Group C functionals). However, even for group A functionals, the devia-

⁴ The results presented in Table III illustrate extreme sensitivity of the results to precise value of the parameters. This is especially true for the parameters related to the σ and ω mesons. This is a reason why in Table II all the parameters are given with six significant digits.

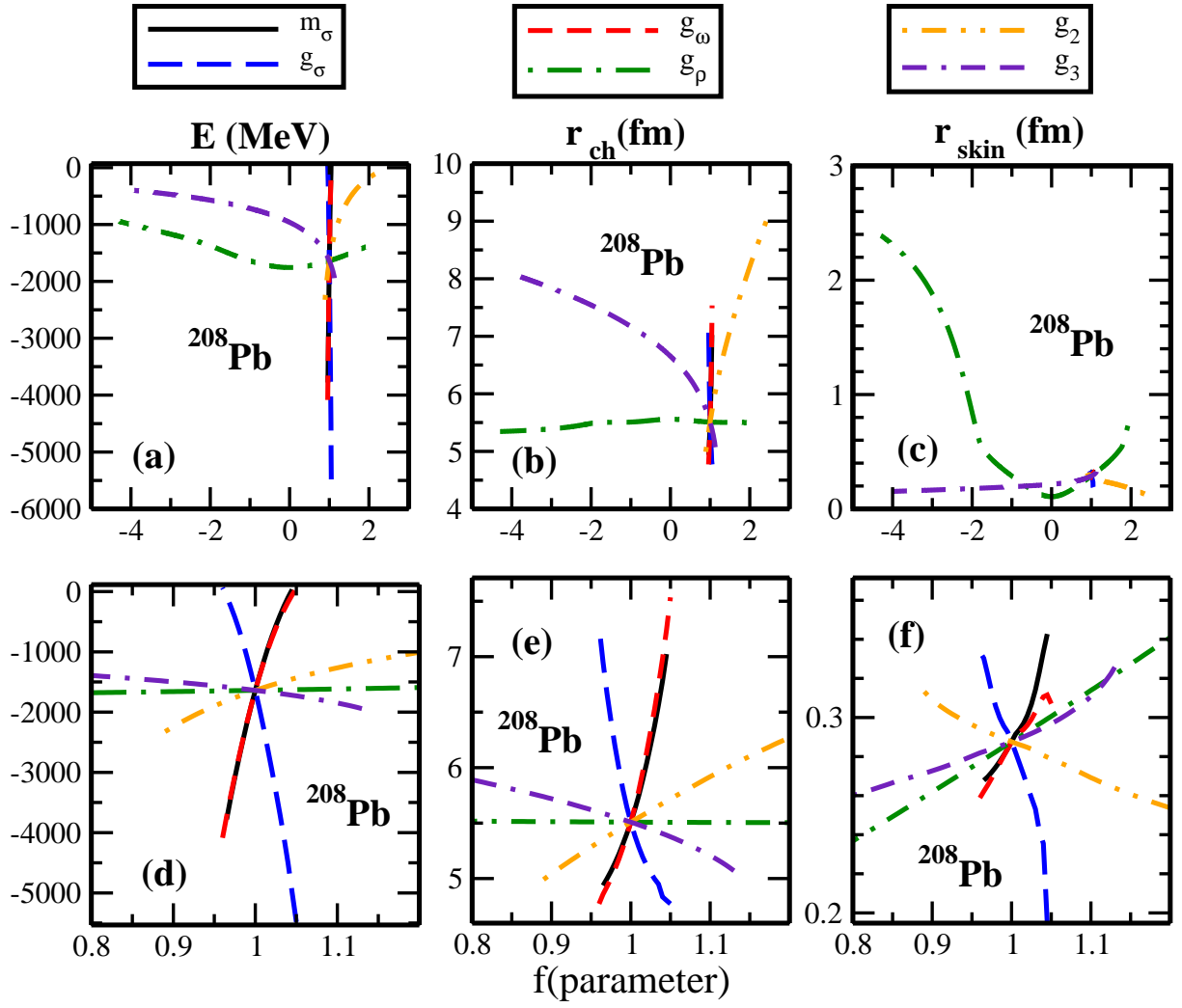


FIG. 1. (Color online) The range of the variations of the parameters of the NL5(C) CEDF and related changes of physical observables such as total binding energy E (left columns), charge radius r_{ch} (central columns) and neutron skin r_{skin} (right columns). Upper row shows the full range of the parameter variations, while the bottom panels magnify the region in the vicinity of optimum parametrization ($f_i = 1.0$). On the one end, the range of parameters is limited by the condition that the total energy of the nucleus is negative. On the other end, it is defined by the collapse of numerical solution due to underlying numerical instabilities. For each line, only the indicated parameter is changing while the remaining parameters are kept at the values corresponding to optimum NL5(C) functional.

tions from mean values reach 10%. The level of localization is even lower for the g_2 and g_3 parameters for which the deviations from the mean values (defined for the set of considered functionals) could reach and even exceed 25% limit (see Fig. 4). However, it is interesting that for the considered functionals the g_3/g_2 ratio is very close to 2.75 (see Fig. 4c). Only two functionals, namely, NLSH and NL5(A), exceed 10% deviation band from the mean value for the g_3/g_2 ratio. Considering that these two parameters define the density dependence of the non-linear meson coupling model, this consistency of the g_3/g_2 ratio over the studied functionals suggests hidden parametric correlations between the g_2 and g_3 parameters.

The 2-dimensional distributions of the parameters of the acceptable functional variations for the NL5(C)

CEDF are presented in Fig. 5. The parameters vary with respect of the central value of the distribution (which are typically given by the parameters of optimum functional) by at most 1.5% for m_σ , 3% for g_σ , 3% for g_ω , 3% for g_ρ , 7% for g_2 and 10% for g_3 . However, these ranges of the parameter variations are dependent on the details of the fitting protocol. For example, in the NL5(A) functional these ranges of the parameter variations are substantially larger for the g_2 and g_3 parameters for which they are around 20% and 40%, respectively (see Fig. 6a). These larger ranges for the g_2 and g_3 parameters in the acceptable NL5(A) functionals as compared with the NL5(C) ones are the consequence of the 4-fold increase of adopted error for K_0 (from 2.5% up to 10% [see Table I]).

The analysis of these distributions can also provide the

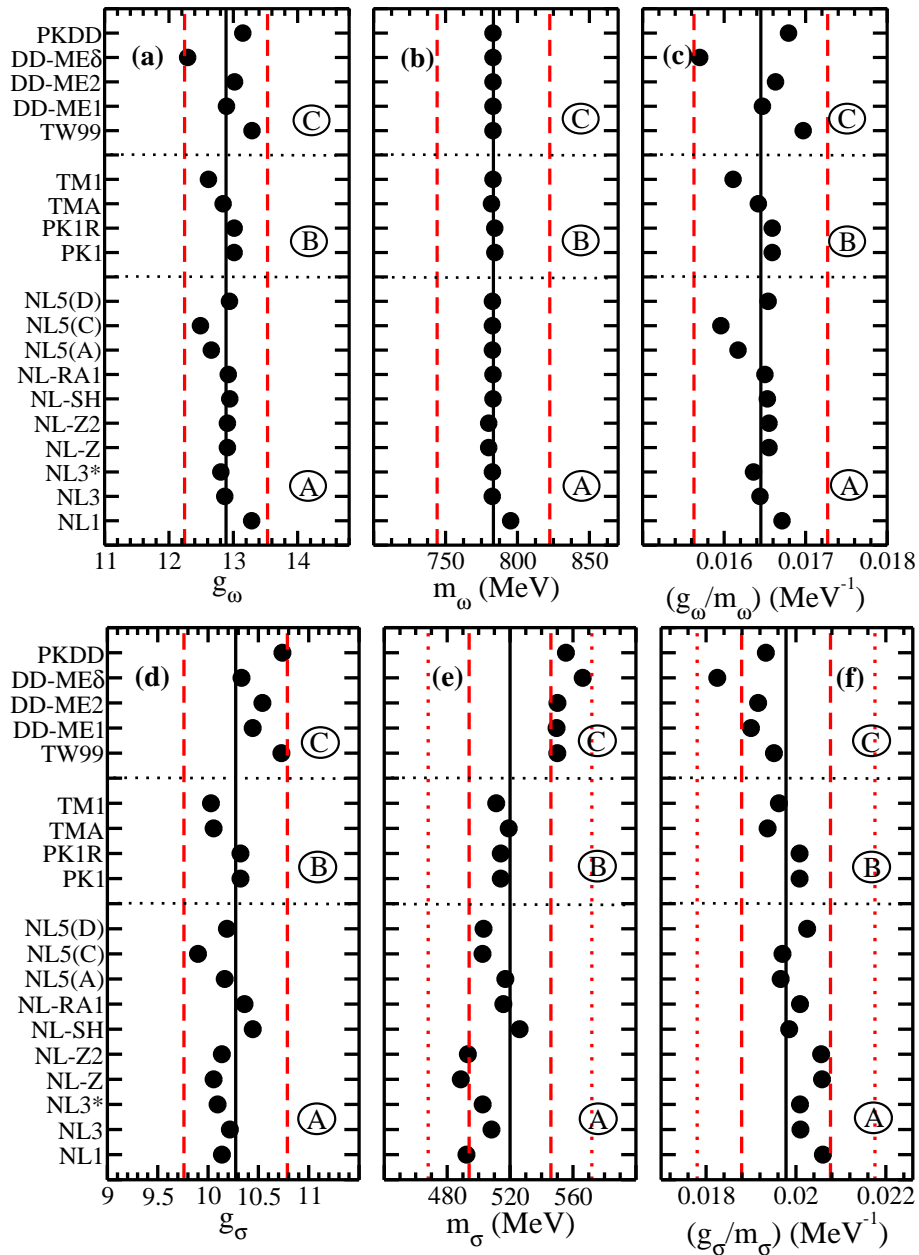


FIG. 2. (Color online) The masses and coupling constants of the σ and ω mesons in different CEDFs which contain meson exchange. They are combined into three groups dependent on how self- and mixed-couplings are introduced. Group A represents the parametrizations which include non-linear self-couplings only for the σ -meson. Group B contains the parametrizations which include self-couplings for the σ - and ω -mesons (and ρ -mesons in the case of PK1R). Group C represents the parametrizations which include density-dependent meson-nucleon couplings for the σ -, ω -, and ρ -mesons. Note that the mass m_ω of the ω -meson is fixed at indicated values in all functionals except NL3, PK1 and PK1R. The parameters are taken from Refs. [46] (NL1), [49] (NL3), [17] (NL3*), [47] (NL-Z), [58] (NL-Z2), [48] (NL-SH), [59] (NL-RA1), [60] (PK1,PK1R), [61] (TMA), [62] (TM1), [19] (TW99), [63] (DD-ME1), [16] (DD-ME2), [64] (DD-ME δ), [60] (PKDD). Note that we omitted mass-dependent terms for g_ω in the TMA parametrization which is a good approximation for heavy nuclei since $g_\omega = 12.842 + 3.191A^{-0.4}$ [61]. Vertical solid lines represent the mean values of the respective parameter over the set of indicated functionals. Red dashed and dotted lines show the $\pm 5\%$ and $\pm 10\%$ deviation bands with respect of these mean values.

information on the presence of non-linear effects which are related either to non-linear dependencies of the observables on the coupling constants or complicated structure of the χ^2 hypersurface exhibiting several separated lo-

cal minima [40]. The position of the optimum functional in the plots of Figs. 5 and 6 corresponds to the crossing point of the $f(par_i) = 1.0$ and $f(par_j) = 1.0$ lines. In absolute majority of the cases the distributions shown in

TABLE III. The factor g by which one has to multiply the indicated parameter of the NL5(C) functional in order to get 10 MeV increase in binding energy of ^{208}Pb . Note that other parameters of the functional are kept at their original values.

Parameter	Factor g
m_σ	0.999801
g_σ	1.000170
g_ω	0.999796
g_ρ	0.992981
g_2	1.002189
g_3	0.997833

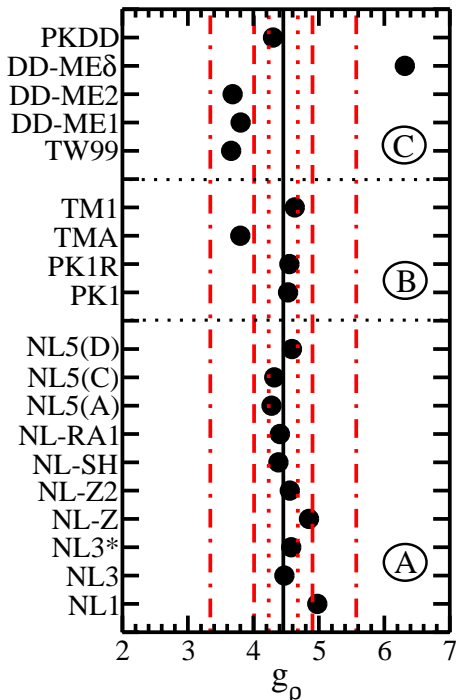


FIG. 3. (Color online) The same as Fig. 2 but for the g_ρ parameter. Red dotted, dashed and dash-dotted lines show the $\pm 5\%$, $\pm 10\%$ and $\pm 25\%$ deviation bands with respect of mean values.

Figs. 5 and 6 have ellipsoid-like shapes with central point of the distribution at this crossing point. This means that non-linear effects are not affecting these distributions. The only exception is the case of the $f(g_3) - f(g_2)$ distribution for the NL5(A) functional in which the optimum functional is located off the center of the distribution (see Fig. 6a).

In addition, the correlations between the parameters of the functional can be easily defined from these distributions. Strong correlations between the m_σ and g_σ parameters are clearly visible in Figs. 5d and 6d. The same is true for the pair of the m_σ and g_ω parameters (see Figs. 5b and 6b). This is not surprising since these parameters enter the definition of the nucleonic potential via the sum of attractive scalar potential S (which

depends on m_σ and g_σ) and repulsive vector potential V (which depends on m_ω and g_σ) [15]. Note that m_ω is fixed at $m_\omega = 782.6$ MeV (see Table II). It is interesting to mention that these strong correlations between the m_σ and g_ω parameters are clearly visible in Figs. 1a, b, d, and e where the modifications of the factors $f(g_\omega)$ and $f(m_\sigma)$ lead to almost the same changes in binding energies and charge radii.

In contrast, the g_ρ parameter does not correlate with other parameters of the functional. This is illustrated in Figs. 5c and 6c where the $f(g_\rho) - f(m_\sigma)$ distributions are plotted. The fact of the absence of the correlations are easy to understand since the g_ρ parameter defines the isovector properties of the functionals while the m_σ parameter the attractive scalar potential S .

The parametric correlations are especially pronounced for the g_2 and g_3 parameters which define the density dependence of the functional via a non-linear meson coupling (see Eq. (8)). Figs. 5a and 6a clearly show that these two parameters are not independent and that the following linear dependence

$$f(g_3) = af(g_2) + b \quad (10)$$

exists. The parameters a and b , defined from $f(g_3) - f(g_2)$ distributions shown in Figs. 5a and 6a, have the following values $a = 1.461276$ and $b = -0.458276$ for NL5(C) and $a = 1.643$ and $b = -0.64693$ for NL5(A). These parametric correlations are more pronounced for the NL5(A) functional for which the $f(g_3) - f(g_2)$ distribution is narrower and more elongated.

The NL5() functionals depends on 6 parameters. The present analysis strongly suggests that its parameter dependence could be reduced to 5 independent parameters, namely, m_σ , g_σ , g_ω , g_ρ , and g_2 if the parametric correlations given in Eq. (10) are taken into account. However, this requires new refit of the functional with linear dependence of Eq. (10) explicitly used in the fitting protocol. An alternative analysis in manifold boundary approximation method (Ref. [65]) has shown that it is possible to reduce the dimension of the parameter hyperspace of the DD-PC1 CEDF from ten parameters to eight without sacrificing the quality of the reproduction of experimental and empirical data. Similar to the NL5() case, this reduction in Ref. [65] takes place in the channel of the functional which defines its density dependence. In the context of the analysis of theoretical uncertainties there is one clear advantage of the reduction of the dimensionality of the parameter hyperspace via the removal of parametric correlations: such reduction leads to the decrease of statistical errors. This was illustrated in Ref. [37] on the example of the study of statistical errors in the single-particle energies and it is discussed for ground state observables in the present manuscript in Sec. V B.

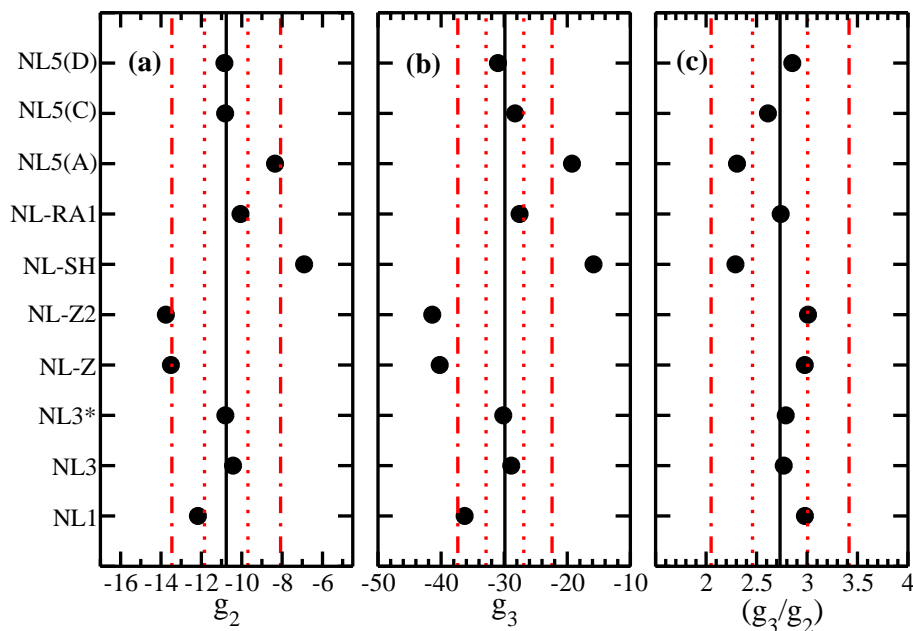


FIG. 4. (Color online) The same as Fig. 2 but for the g_2 and g_3 parameters. Red dotted and dash-dotted lines show the $\pm 10\%$ and $\pm 25\%$ deviation bands with respect of the mean values. Note that only the functionals which belong to group A are considered here.

V. STATISTICAL ERRORS IN THE GROUND STATE OBSERVABLES OF EVEN-EVEN NUCLEI.

A. The case of the NL5(C) functional

In this section we will investigate statistical errors in the description of the ground state properties of spherical Ca, Ni, Sn and Pb even-even isotopes. Within the isotope chain the calculations cover all nuclei between the two-proton and two-neutron drip lines. When possible the statistical errors obtained in the present study will be compared with systematic uncertainties defined in Refs. [3, 31]. In addition, they will be compared with statistical errors obtained in the Skyrme DFT study with UNEDF0 functional of Ref. [6].

Statistical errors in binding energies obtained with the CEDF NL5(C) and their propagation with the neutron number are shown in Fig. 7a. They are close to adopted errors of the fitting protocol [0.1% of binding energy (see Table I)] for the nuclei used in the fit. With increasing isospin the statistical errors in binding energies substantially increase reaching ~ 2.6 , ~ 2.6 , ~ 5.0 and ~ 6.0 MeV at the two-neutron drip line in the Ca, Ni, Sn and Pb isotope chains, respectively. However, they are significantly smaller at the neutron-drip line than those obtained in the Skyrme DFT studies of Ref. [6]; by factors 4.6, 3.1, 3.4 and 2.3 for the Ca, Ni, Sn and Pb isotopes, respectively. Statistical errors in binding energies of these nuclei are by a factor 2-3 smaller than systematic uncertainties in the binding energies obtained in Ref. [3] (see Fig. 8 in this reference). Note that the estimate

of systematic uncertainties of Ref. [3] are based only on four CEDFs, namely, NL3*, DD-PC1, DD-ME2 and DD-ME δ . The investigation of Ref. [28] suggests that the addition of the PC-PK1 functional could lead to a substantial increase of systematic uncertainties in binding energies. This is at least a case for the Yb ($Z = 70$) isotopes for which they increase by a factor of 2.1 when the PC-PK1 results are added (see Fig. 3 in Ref. [31]).

Statistical errors in charge radii r_{ch} are presented in Fig. 7b. They are in the vicinity of 0.1% of the calculated r_{ch} values shown in Fig. 23 of Ref. [3]. For the nuclei used in the fitting protocol, statistical errors are below the adopted errors of 0.2% for r_{ch} . Calculated statistical errors are below 25% of the rms deviations Δr_{ch}^{rms} between calculated and experimental charge radii, which are typical for the state-of-the-art CEDFs and which are shown in Table VI of Ref. [3]. Systematic uncertainties in the predictions of charge radii of the Ca and Ni isotopes obtained from the set of the four functionals (see Fig. 24 of Ref. [3]) are substantially larger (on average, by an approximate factor of 8 and 10, respectively) than relevant statistical errors. This difference goes down with the increase of proton number. For example, the situation in the Pb isotopes depends on the neutron number N . Statistical errors are only somewhat smaller than systematic uncertainties in the Pb nuclei with $N \sim 110$ and $N \sim 126$. On the other hand, they are smaller than statistical uncertainties by a factor of approximately 10 for the nuclei with $N \sim 102$. On average, for the Pb nuclei the statistical errors in charge radii are by a factor of approximately 4 smaller than relevant systematic uncertainties. Similar situation is observed also in the

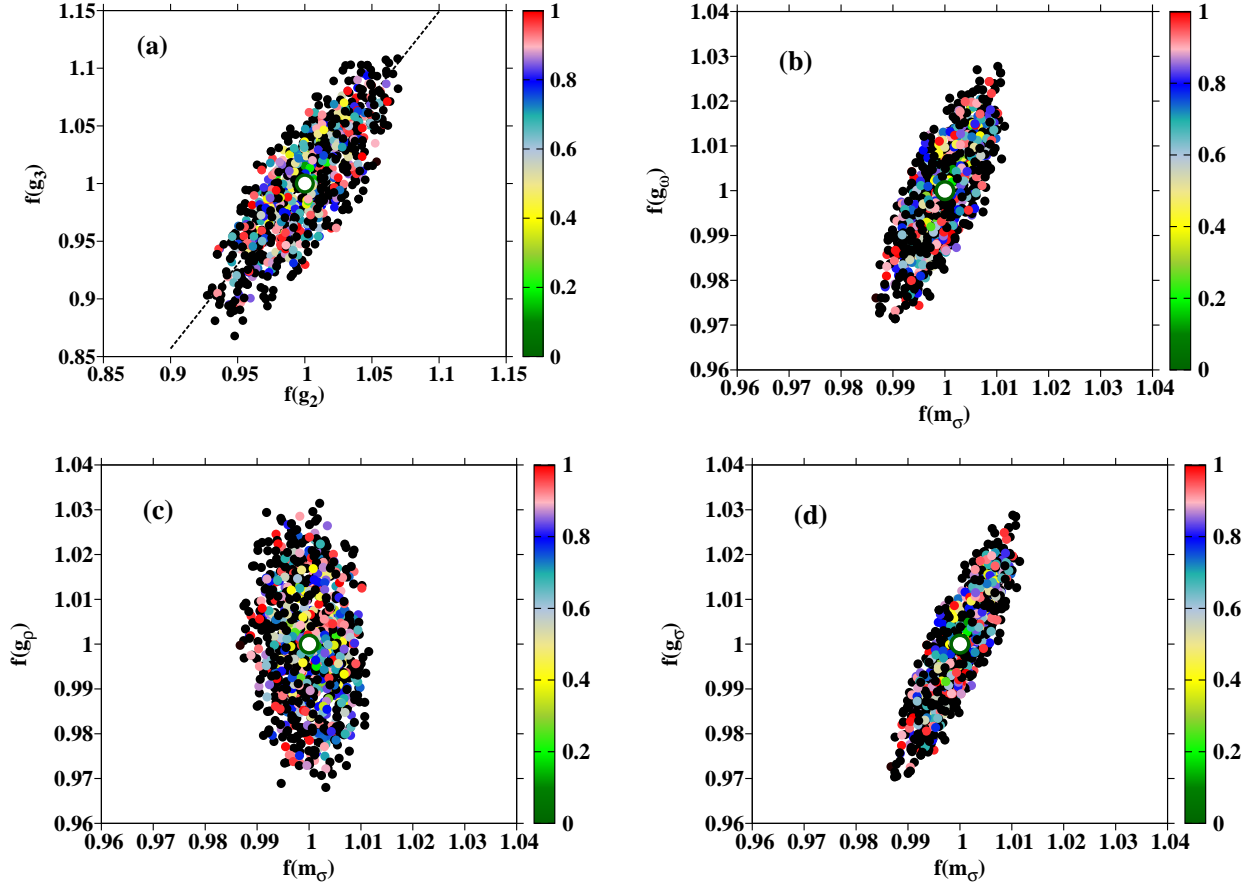


FIG. 5. (Color online) Two-dimensional projections of the distribution of the functional variations in the 6-dimensional parameter hyperspace. The colors indicate the a value of the $\chi_{norm}^2(\mathbf{p})$ of the functional variation where the latter is expressed as $\chi_{norm}^2(\mathbf{p}) = \chi_{norm}^2(\mathbf{p}_0) + a$. The colormap is used for the functional variations with $a \leq 1.0$; there are 500 such variations. Note that it was found in the studies that further increase of the number of functional variations does not change the results for statistical errors. In addition, black circles are used for the functionals with $1.0 < a \leq 1.25$. The optimum functional is shown by large open symbol. The dashed line in panel (a) shows the parametric correlations between g_2 and g_3 parameters defined by Eq. (10).

Sn isotopes, but the average difference between statistical errors and statistical uncertainties in charge radii is of the order of 7.

Contrary to Skyrme DFT calculations with the UNEDF0 functional (see Fig. 4b in Ref. [6]), statistical errors in charge radii calculated with NL5(C) (see Fig. 7b in the present paper) do not show significant increase with neutron number. In reality, the $\sigma(r_{ch})$ values obtained with NL5(C) for the Sn and Pb isotopes show very modest increase of approximately 20% on going from two-proton to two-neutron drip line. Note that the $\sigma(r_{ch})$ values show some fluctuations as a function of neutron number which are due to underlying shell structure; they become especially pronounced in the Ni isotopes. While statistical errors for charge radii of the Ca, Ni and Sn isotopes are comparable for Skyrme UNEDF0 and CDFT NL5(C) calculations for the nuclei near two-proton drip line, the situation changes drastically with the increase of neutron number so that for the Ca, Ni, Sn and Pb

nuclei at the two-neutron drip line the $\sigma(r_{ch})$ values obtained in Skyrme calculations are by factor of 17-33 larger than those obtained in CDFT calculations with CEDF NL5(C).

Statistical errors in two-neutron separation energies are displayed in Fig. 7c. They are typically in the range of 0.1 - 0.3 MeV and do not show a clear tendency of the increase on approaching two-neutron drip line. These statistical errors show substantial fluctuations as a function of neutron number with the changes in the slope of $\sigma(S_{2n})$ typically taking place in the vicinity of the shell ($N = 20, 28, 50, 82$ and 126) and subshell ($N = 40$) closures. The calculated $\sigma(S_{2n})$ values are typically by a factor of 3-4 smaller than the rms-deviations between theory and experiment for the state-of-the-art CEDF (see Table III in Ref. [3]). It is interesting to compare our results with the ones obtained in Skyrme DFT calculations of Ref. [6]. While the $\sigma(S_{2n})$ values are comparable for both models in the vicinity of the β -stability line, they

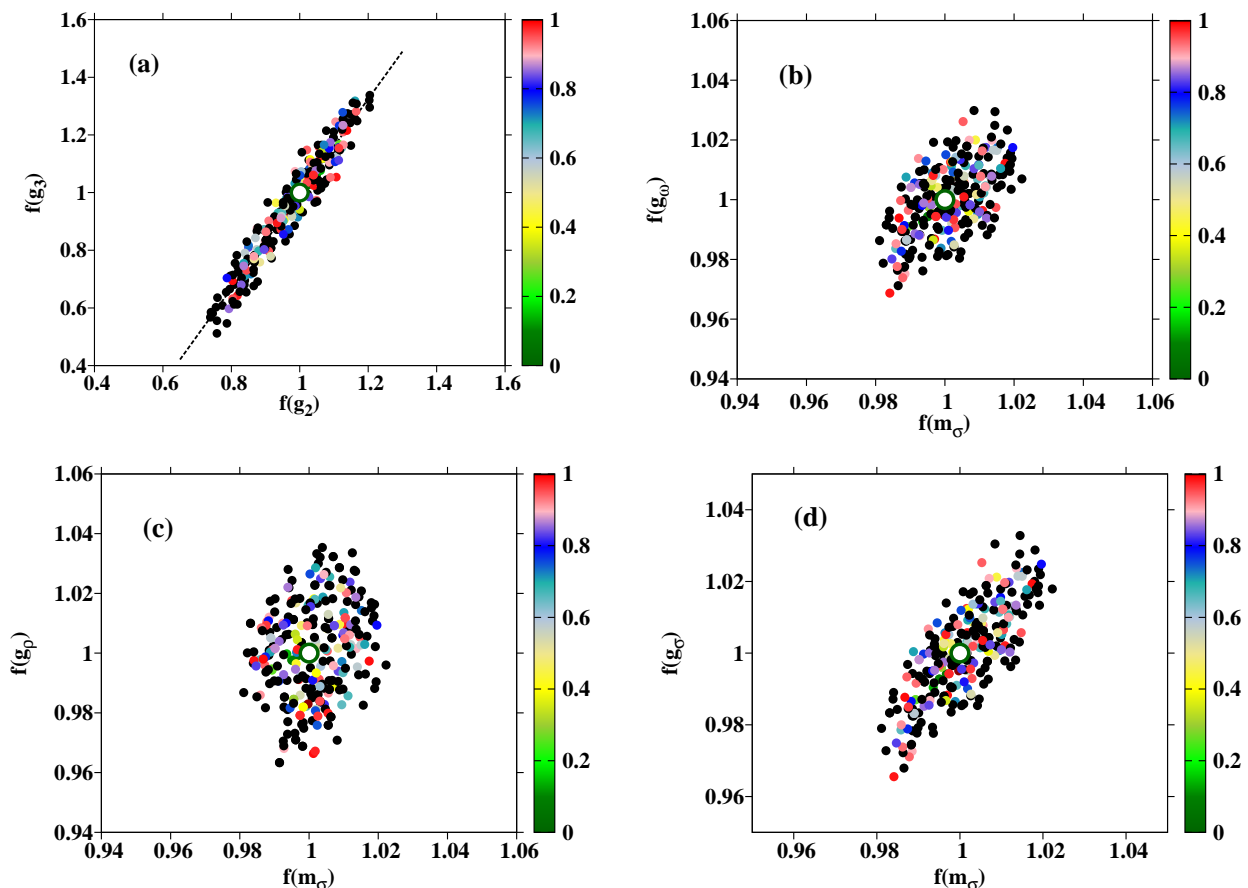


FIG. 6. (Color online) The same as Fig. 5 but for the NL5(A) functional. Considering the increase of the size of the parameter hyperspace and extremely time-consuming nature of numerical calculations only 150 functional variations satisfying the condition of Eq. (4) have been collected. This leads to some reduction of the accuracy of the calculations of statistical errors. However, the analysis of the NL5(C) results for which 500 acceptable functional variations have been collected allows to conclude that statistical errors obtained with the 150 functional variations differ from those calculated with 500 variations only by approximately 5%.

increase drastically with increasing neutron number in the Skyrme DFT calculations approaching ~ 1.4 , ~ 1.4 , ~ 0.8 and ~ 0.75 MeV for Ca, Ni, Sn and Pb nuclei at the two-neutron drip line, respectively. This trend is contrary to the one seen in the CDFT results.

Statistical errors in the neutron skin thickness r_{skin} are shown in Fig. 7d. They are close to zero near the $N = Z$ line but increase with increasing neutron number. This increase is rapid in the Ca, Ni and Sn isotopes but it is more moderate in the Pb isotopes. An interesting feature of the latter chain is the decrease of the $\sigma(r_{skin})$ values above $N \sim 170$ which is most likely due to underlying shell effects. The statistical errors in the neutron skin thickness are substantially larger in the Skyrme DFT calculations with the UNEDF0 and SV-min functionals (Ref. [66]) than in the present RHB calculations with CEDF NL5(C). For example, for ^{208}Pb the $\sigma(r_{skin})$ values are 0.058 fm, 0.037 fm and 0.0035 fm in the calculations with the UNEDF0, SV-min and NL5(C) functionals, respectively. In the neutron-rich Ca isotopes

near the two-neutron drip line the $\sigma(r_{skin})$ values obtained in non-relativistic calculations are by a factor of approximately 7 larger than those obtained in the relativistic ones. The statistical errors in the neutron skin thickness shown in Fig. 7d are substantially smaller than systematic uncertainties shown in Fig. 25 of Ref. [3]. In the vicinity of the two-neutron drip line, the latter ones reach 0.15 fm, 0.2 fm, 0.25 fm and 0.25 fm in the neutron rich Ca, Ni, Sn and Pb nuclei, respectively.

B. The impact of the details of the fitting protocol and of soft parameters on statistical errors.

It is important to understand how the details of the fitting protocol could affect the statistical errors in physical observables of interest. Considering the ingredients entering into fitting protocol and the uncertainties in the definition of empirical/experimental values of physical observables and adopted errors, the complete answer

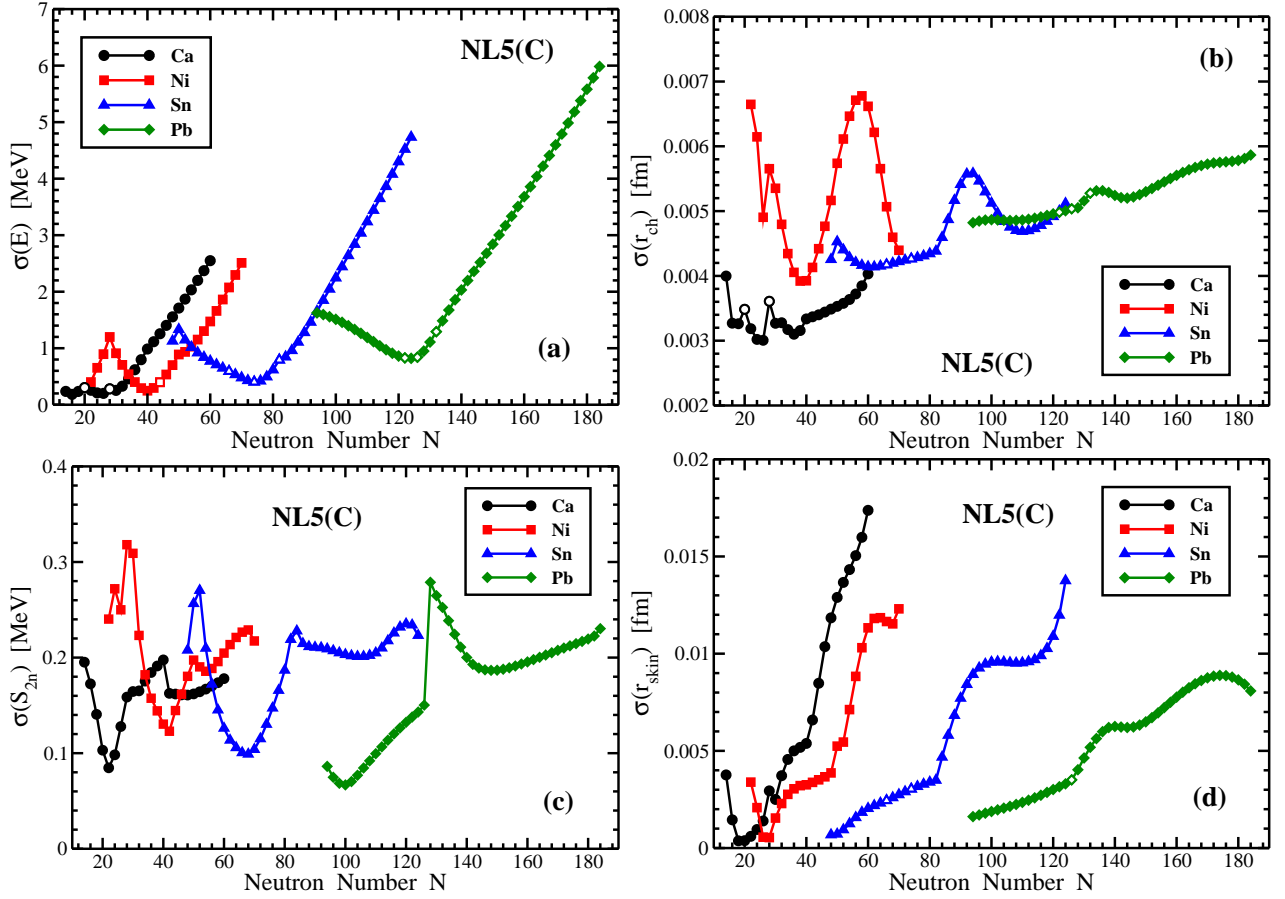


FIG. 7. (Color online) The propagation of statistical errors in binding energies [panel (a)], charge radii [panel (b)], two-neutron separation energies [panel (c)] and neutron skins [panel (d)] with neutron number. The results are presented for the Ca ($Z = 20$), Ni ($Z = 28$), Sn ($Z = 50$) and Pb ($Z = 82$) isotopes between two-proton and two-neutron drip lines. Open symbols are used to indicate the nuclei whose experimental data of the type shown on the vertical axis of the panel has been used in the fitting protocol of the NL5(C) functional.

to this question requires enormous amount of numerical calculations which are beyond the scope of the present investigation. However, in order to get a crude estimate of potential changes in statistical errors additional calculations have been performed for the two cases discussed below.

In the first case, we analyse statistical errors obtained with the NL5(A) functional. This functional differs from the NL5(C) one by an increased adopted error for K_0 and the presence of neutron skin of ^{90}Zr in the fitting protocol (see Table I). As a consequence of these features, the acceptable NL5(A) functionals show larger range of variations for the g_2 and g_3 parameters as compared with the NL5(C) ones (compare Figs. 5a and 6a). This leads to some increase in statistical errors for binding energies (especially in neutron-rich nuclei in which the $\sigma(E)$ values are increased by $\sim 30\%$ as compared with the NL5(C) results) and two-neutron separation energies (see Figs. 8a, e, d and h). On the contrary, as compared with the NL5(C) results statistical errors in neutron skin are only slightly increased (see Fig. 8c and g) and statistical er-

rors in charge radii even decrease in the Pb isotopes and for some Ca isotopes (see Fig. 8b and f).

Despite these changes statistical errors for physical observables of interest obtained with the NL5(A) functional still remain substantially smaller than those obtained in Skyrme DFT calculations (compare results presented in this subsection with the discussion in Sec. V A).

In the second case, we use the NL5(C) functional but fix the g_2 , g_3 and g_ρ parameters at the values of the optimal functional during the Monte-Carlo procedure. As shown in Secs. III and IV, the g_σ , m_σ and g_ω parameters, which are allowed to change during Monte-Carlo procedure, are well localized in the parameter hyperspace and they vary in a very narrow range with respect of the optimum functional. Fig. 8 compares the results for the Ca and Pb nuclei presented in Fig. 7 with statistical errors obtained in such calculations. The freezing of the g_2 , g_3 and g_ρ parameters in the functional leads to a substantial decrease of statistical errors in binding energies of neutron-rich nuclei so that in two-neutron drip line nuclei they are only by a factor of approximately two larger

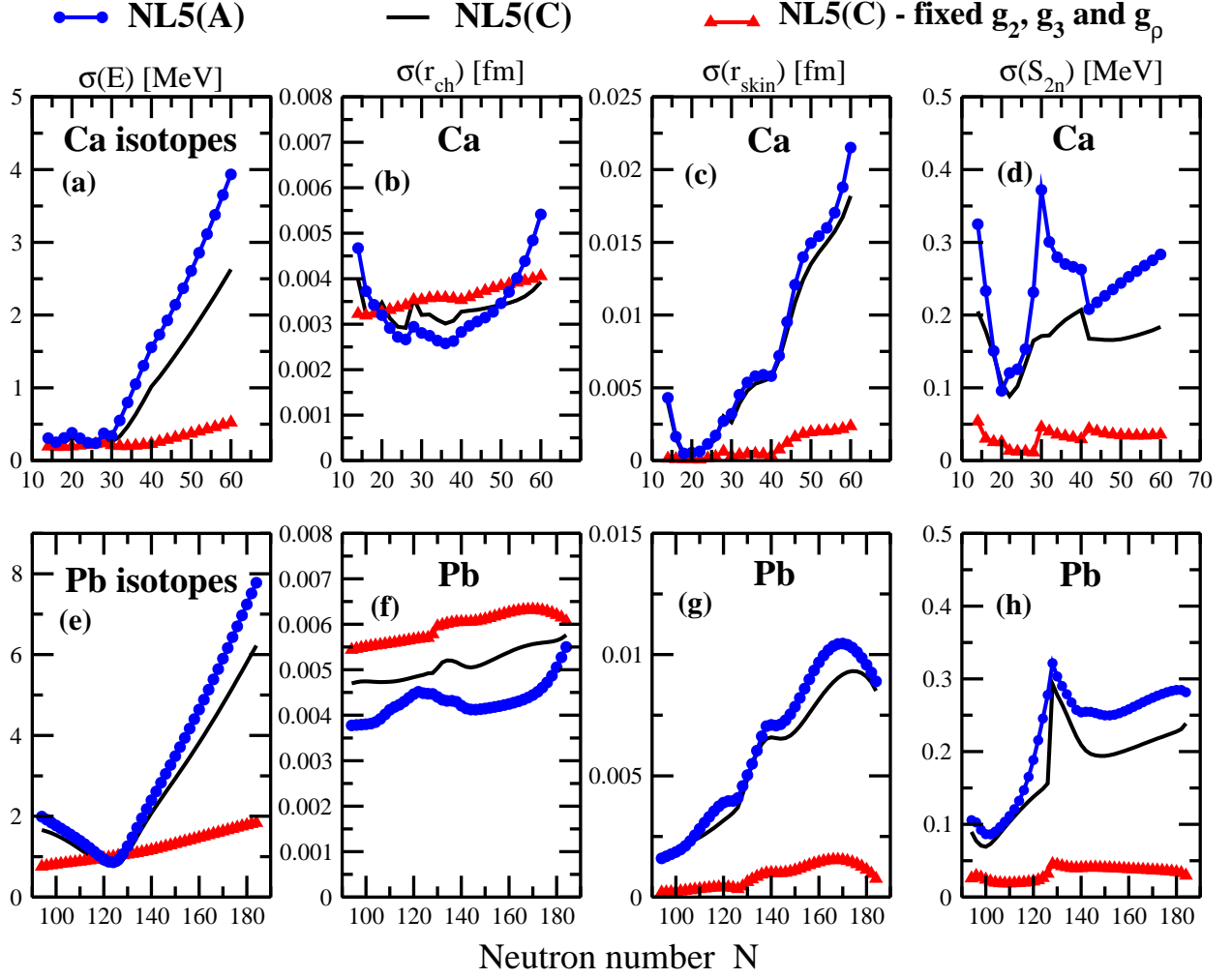


FIG. 8. (Color online) The propagation of statistical errors for the binding energies ($\sigma(E)$), charge radii ($\sigma(r_{ch})$), neutron skins ($\sigma(r_{skin})$) and two-neutron separation energies ($\sigma(S_{2n})$) in the Ca and Pb isotope chains. The results of the calculations with the NL5(C) and NL5(A) functionals are shown by solid black line and blue solid line with solid circles, respectively. In addition, red triangle symbols show statistical errors for the NL5(C) functional under the condition that the g_ρ , g_2 and g_3 parameters are fixed at the values corresponding to optimum NL5(C) functional.

than those for the nuclei used in the fitting protocol (Fig. 8a and e). Note that the $\sigma(E)$ values obtained in such calculations are typically significantly smaller (especially in very neutron-rich nuclei) than those obtained in full NL5(C) calculations shown by solid black line. The only exception is the region of neutron numbers in which the experimental data on binding energies was used in the fitting protocol. Statistical errors in two-neutron separation energies become very small ($\sigma(S_{2n}) < 0.05$ MeV) in the calculations with fixed g_2 , g_3 and g_ρ parameters (see Fig. 8d and h). They are also significantly smaller than those obtained in full NL5(C) calculations. Simultaneous freezing of the g_2 , g_3 and g_ρ parameters leads to a substantial decrease of statistical errors in neutron skin so that in the most of the nuclei they are very close to zero (see Fig. 8c and g). On the contrary, the impact of freezing of the g_2 , g_3 and g_ρ parameters on statisti-

cal errors in charge radii is very limited (see Fig. 8b and f)). It is interesting that it leads to slight increase of the $\sigma(r_{ch})$ as compared with those obtained in full NL5(C) calculations.

This analysis clearly illustrates the importance of the discrimination of the impact of the *stiff* and *soft* parameters of CEDFs on statistical errors. Such a separation of the parameters into two types was discussed in Ref. [65]. Even when the parameters of nuclear EDFs are adjusted to experimental/empirical/pseudo data, their predictions are sensitive to only a few combinations of parameters (*stiff* parameter combinations) and exhibit an exponential decrease of sensitivity to variations of the remaining *soft* parameters that are only approximately constrained by data. In non-linear meson coupling models, the stiff parameters are represented by m_ω , g_ω and g_σ . Their contribution to statistical errors is rather small and mostly

independent of neutron number. On the contrary, the combination of soft parameters g_2 , g_3 and g_ρ leads to a significant increase of statistical errors for binding energies and neutron skins on approaching two-neutron drip line. They also lead to an increase of statistical errors in two-neutron separation energies. Thus, one can conclude that the presence of soft parameters in the CEDFs is the major source of statistical errors.

VI. STATISTICAL ERRORS IN THE SINGLE-PARTICLE ENERGIES

TABLE IV. Neutron and proton single-particle states in the ^{208}Pb nucleus. Columns 2 and 5 show the mean energies \bar{e}_i [in MeV] of these states obtained in the calculations with CEDF NL5(C). Columns 3 and 6 show their standard deviations $\sigma(e_i)$ [in MeV]. The positions of the proton and neutron Fermi levels are indicated.

Neutron			Proton		
Orbital	\bar{e}_ν	$\sigma(e_\nu)$	Orbital	\bar{e}_π	$\sigma(e_\pi)$
1	2	3	4	5	6
$1s_{1/2}$	-58.257	0.424	$1s_{1/2}$	-47.100	0.401
$1p_{3/2}$	-52.142	0.376	$1p_{3/2}$	-41.573	0.360
$1p_{1/2}$	-51.581	0.363	$1p_{1/2}$	-40.933	0.345
$1d_{5/2}$	-44.809	0.316	$1d_{5/2}$	-34.691	0.307
$1d_{3/2}$	-43.497	0.282	$1d_{3/2}$	-33.249	0.270
$2s_{1/2}$	-40.566	0.241	$2s_{1/2}$	-29.725	0.221
$1f_{7/2}$	-36.614	0.252	$1f_{7/2}$	-26.864	0.251
$1f_{5/2}$	-34.228	0.189	$1f_{5/2}$	-24.320	0.187
$2p_{3/2}$	-30.515	0.149	$2p_{3/2}$	-20.045	0.150
$2p_{1/2}$	-29.526	0.128	$2p_{1/2}$	-19.054	0.136
$1g_{9/2}$	-27.862	0.191	$1g_{9/2}$	-18.402	0.199
$1g_{7/2}$	-24.177	0.112	$1g_{7/2}$	-14.556	0.128
$2d_{5/2}$	-20.708	0.098	$2d_{5/2}$	-10.465	0.122
$2d_{3/2}$	-19.127	0.091	$1h_{11/2}$	-9.544	0.159
$1h_{11/2}$	-18.809	0.141	$2d_{3/2}$	-8.903	0.121
$3s_{1/2}$	-18.301	0.095	$3s_{1/2}$	-7.729	0.121
Proton Fermi level					
$1h_{9/2}$	-13.774	0.108	$1h_{9/2}$	-4.367	0.134
$2f_{7/2}$	-11.320	0.085	$2f_{7/2}$	-1.107	0.120
$1i_{13/2}$	-9.661	0.104	$1i_{13/2}$	-0.481	0.133
$2f_{5/2}$	-9.390	0.098	$2f_{5/2}$	0.802	0.131
$3p_{3/2}$	-8.591	0.087	$3p_{3/2}$	2.133	0.121
$3p_{1/2}$	-7.895	0.090	$3p_{1/2}$	2.828	0.125
Neutron Fermi level					
$1i_{11/2}$	-3.515	0.148			
$2g_{9/2}$	-2.688	0.080			
$3d_{5/2}$	-0.873	0.062			
$2g_{7/2}$	-0.855	0.090			
$4s_{1/2}$	-0.599	0.050			
$1j_{15/2}$	-0.597	0.081			
$3d_{3/2}$	-0.281	0.061			
$4p_{3/2}$	2.557	0.018			
$4p_{1/2}$	2.669	0.019			

The energies of the single-particle states e_i represent another quantity which affects many physical observables (see Refs. [21, 28, 29, 34, 67]). In this section we investigate statistical errors in the description of the energies

TABLE V. The same as Table IV but for the ^{266}Pb nucleus. The states in the energy range from ~ -42 MeV up to ~ -20 MeV are omitted in order to simplify the table.

Neutron			Proton		
Orbital	\bar{e}_ν	$\sigma(e_\nu)$	Orbital	\bar{e}_π	$\sigma(e_\pi)$
1	2	3	4	5	6
$1s_{1/2}$	-53.045	0.364	$1s_{1/2}$	-49.945	0.323
$1p_{3/2}$	-47.922	0.333	$1p_{3/2}$	-45.498	0.304
$1p_{1/2}$	-47.567	0.326	$1p_{1/2}$	-45.070	0.297
Proton Fermi level					
$2d_{3/2}$	-20.427	0.153	$1h_{11/2}$	-18.396	0.199
$3s_{1/2}$	-19.619	0.153	$2d_{3/2}$	-18.075	0.176
$1h_{11/2}$	-19.595	0.188	$3s_{1/2}$	-16.727	0.169
Proton Fermi level					
$1h_{9/2}$	-16.052	0.159	$1h_{9/2}$	-14.726	0.186
$2f_{7/2}$	-13.384	0.142	$2f_{7/2}$	-10.867	0.172
$2f_{5/2}$	-11.882	0.138	$1i_{13/2}$	-10.415	0.184
$1i_{13/2}$	-11.638	0.163	$2f_{5/2}$	-9.372	0.182
$3p_{3/2}$	-11.057	0.130	$3p_{3/2}$	-7.655	0.171
$3p_{1/2}$	-10.494	0.128	$3p_{1/2}$	-7.086	0.177
$1i_{11/2}$	-7.153	0.161	$1i_{11/2}$	-5.779	0.198
$2g_{9/2}$	-5.728	0.124	$2g_{9/2}$	-2.583	0.174
$2g_{7/2}$	-4.138	0.123	$1j_{15/2}$	-2.234	0.175
$3d_{5/2}$	-3.847	0.100	$2g_{7/2}$	-0.896	0.186
$1j_{15/2}$	-3.691	0.143	$3d_{5/2}$	0.851	0.168
$4s_{1/2}$	-3.342	0.088	$3d_{3/2}$	1.540	0.173
$3d_{3/2}$	-3.252	0.097	$4s_{1/2}$	2.130	0.162
Neutron Fermi level					
$2h_{11/2}$	1.038	0.096	$1j_{13/2}$	3.185	0.216
$4p_{3/2}$	1.292	0.034			
$1j_{13/2}$	1.406	0.164			
$4p_{1/2}$	1.460	0.033			
$3f_{7/2}$	1.546	0.051			
$3f_{5/2}$	1.998	0.045			
$2h_{9/2}$	2.387	0.086			

of the single-particle states e_i ; they are quantified by the standard deviations $\sigma(e_i)$. We focus on three nuclei, namely, ^{208}Pb , ^{266}Pb and $^{304}120$. The first one is well known doubly magic nucleus which serves as a testing ground in many theoretical studies. Second nucleus is the last bound neutron-rich Pb isotope in absolute majority of theoretical studies (see Fig. 14 in Ref. [3]); it is characterized by large $N = 184$ shell gap (see Fig. 6a in Ref. [28]). Third nucleus is the $Z = 120$, $N = 184$ superheavy nucleus which is considered as doubly magic in a number of studies (see, for example, Ref. [58]); this conclusion is however model dependent (see Refs. [29, 58, 68, 69] and references quoted therein). The comparison of the results obtained for these three nuclei will allow to assess the propagation of statistical errors on going from the valley of beta-stability towards the extremes of neutron number and charge.

Tables IV, V and VI show the calculated mean energies \bar{e}_i of the single-particle states and related standard deviations $\sigma(e_i)$ obtained in these nuclei. The general trend, which is clearly seen in these tables, is the decrease of statistical errors on going from the bottom of nucleonic po-

TABLE VI. The same as Table IV but for the $^{304}120$ nucleus. Neutron states in the energy range from ~ -50 MeV up to ~ -25 MeV and proton states in the energy range from ~ -35 MeV up to ~ -12 MeV are omitted in order to simplify the table.

Neutron			Proton		
Orbital	\bar{e}_ν	$\sigma(e_\nu)$	Orbital	\bar{e}_π	$\sigma(e_\pi)$
1	2	3	4	5	6
$1s_{1/2}$	-57.748	0.386	$1s_{1/2}$	-41.480	0.367
$1p_{3/2}$	-53.698	0.362	$1p_{3/2}$	-37.545	0.349
$1p_{1/2}$	-53.459	0.359	$1p_{1/2}$	-37.246	0.343
—	—	—	—	—	—
$3s_{1/2}$	-24.421	0.107	$3s_{1/2}$	-9.349	0.134
$1h_{9/2}$	-23.315	0.105	$1h_{9/2}$	-8.169	0.126
$2f_{7/2}$	-19.452	0.098	$1i_{13/2}$	-4.150	0.153
$1i_{13/2}$	-18.893	0.132	$2f_{7/2}$	-3.903	0.123
$2f_{5/2}$	-17.953	0.092	$2f_{5/2}$	-2.418	0.121
—	—	—	Proton Fermi level		
$3p_{3/2}$	-15.293	0.092	$3p_{3/2}$	-0.302	0.132
$3p_{1/2}$	-14.947	0.093	$3p_{1/2}$	0.017	0.134
$1i_{11/2}$	-14.288	0.103	$1i_{11/2}$	0.612	0.130
$2g_{9/2}$	-11.194	0.086	$1j_{15/2}$	3.758	0.133
$1j_{15/2}$	-10.809	0.103	$2g_{9/2}$	4.230	0.119
$2g_{7/2}$	-9.206	0.099	—	—	—
$3d_{5/2}$	-7.336	0.085	—	—	—
$3d_{3/2}$	-7.014	0.085	—	—	—
$4s_{1/2}$	-6.372	0.077	—	—	—
Neutron Fermi level					
$1j_{13/2}$	-5.195	0.136	—	—	—
$2h_{11/2}$	-3.278	0.084	—	—	—
$1k_{17/2}$	-2.669	0.084	—	—	—
$2h_{9/2}$	-1.227	0.100	—	—	—
$3f_{7/2}$	-0.626	0.066	—	—	—
$3f_{5/2}$	-0.188	0.067	—	—	—
$4p_{3/2}$	0.080	0.051	—	—	—
$4p_{1/2}$	0.259	0.052	—	—	—
$5s_{1/2}$	2.353	0.016	—	—	—
$4d_{5/2}$	2.822	0.017	—	—	—

tential towards continuum. The states at the bottom of potential are characterized by $\sigma(e_i) \sim 0.35$ MeV both for proton and neutron subsystems for all nuclei under consideration. In ^{208}Pb , the neutron and proton states are characterized by $\sigma(e_i) \sim 0.1$ MeV in the vicinity of the respective Fermi levels which have similar energies. The addition of neutrons leading to ^{266}Pb moves the proton Fermi level to lower energies (deeper into the potential) and neutron Fermi level closer to continuum limit. As a consequence, the $\sigma(e_i)$ values for the proton states in the vicinity of the proton Fermi level increase to ~ 0.15 MeV (see Table V). On the contrary, with the exception of the high- j $\nu 1j_{15/2}$ and $\nu 1j_{13/2}$ states for which $\sigma(e_i) \sim 0.15$ MeV, the $\sigma(e_i)$ values for the neutron states in the vicinity of the neutron Fermi level is less than 0.1 MeV (see Table V). Because the neutron and proton Fermi levels are located at ~ -6.4 MeV and ~ -2.4 MeV, respectively, in the $^{184}120$ nucleus [which is not far away from their values in ^{208}Pb], the $\sigma(e_i)$ values for the single-particle states in this nucleus are comparable with the

ones in ^{208}Pb (compare tables IV and VI).

TABLE VII. Relative energies $\Delta e_i(m, j) = e_i(m) - e_i(j)$ of the pairs of neutron ($i = \nu$) and proton ($i = \pi$) single-particle states in the ^{208}Pb nucleus. The pairs of neighboring states m and j shown in the columns 1 and 4 are defined from the single-particle spectra obtained with the NL5(C) CEDF. The columns 2 and 5 show their mean relative energies $\overline{\Delta e}_i(m, j)$ [in MeV] while the columns 3 and 6 show standard deviations $\sigma(\Delta e_i(m, j))$ [in MeV]. All the pairs of the states up to the label “proton/neutron Fermi level” have both members located below respective Fermi levels. Next line after this statement indicates the pair of the states one of the members of which is located below the large shell gap (either proton $Z = 82$ or neutron $N = 126$ one) and another above this gap. Subsequent lines show the pairs of the states both members of which are located above respective Fermi levels (above proton $Z = 82$ or neutron $N = 126$ shell gaps).

Neutron			Proton		
Orbital pairs (m, j)	$\overline{\Delta e}_\nu$	$\sigma(\Delta e_\nu)$	Orbital pairs (m, j)	$\overline{\Delta e}_\pi$	$\sigma(\Delta e_\pi)$
1	2	3	4	5	6
$1s_{1/2} - 1p_{3/2}$	6.115	0.054	$1s_{1/2} - 1p_{3/2}$	5.527	0.049
$1p_{3/2} - 1p_{1/2}$	0.560	0.013	$1p_{3/2} - 1p_{1/2}$	0.640	0.016
$1p_{1/2} - 1d_{5/2}$	6.772	0.053	$1p_{1/2} - 1d_{5/2}$	6.242	0.045
$1d_{5/2} - 1d_{3/2}$	1.313	0.037	$1d_{5/2} - 1d_{3/2}$	1.442	0.042
$1d_{3/2} - 2s_{1/2}$	2.931	0.047	$1d_{3/2} - 2s_{1/2}$	3.524	0.058
$2s_{1/2} - 1f_{7/2}$	3.951	0.033	$2s_{1/2} - 1f_{7/2}$	2.860	0.049
$1f_{7/2} - 1f_{5/2}$	2.386	0.073	$1f_{7/2} - 1f_{5/2}$	2.545	0.079
$1f_{5/2} - 2p_{3/2}$	3.713	0.055	$1f_{5/2} - 2p_{3/2}$	4.274	0.063
$2p_{3/2} - 2p_{1/2}$	0.989	0.028	$2p_{3/2} - 2p_{1/2}$	0.991	0.028
$2p_{1/2} - 1g_{9/2}$	1.664	0.090	$2p_{1/2} - 1g_{9/2}$	0.652	0.106
$1g_{9/2} - 1g_{7/2}$	3.685	0.116	$1g_{9/2} - 1g_{7/2}$	3.846	0.121
$1g_{7/2} - 2d_{5/2}$	3.469	0.051	$1g_{7/2} - 2d_{5/2}$	4.092	0.058
$2d_{5/2} - 2d_{3/2}$	1.581	0.039	$2d_{5/2} - 1h_{11/2}$	0.920	0.098
$2d_{3/2} - 1h_{11/2}$	0.318	0.122	$1h_{11/2} - 2d_{3/2}$	0.641	0.133
$1h_{11/2} - 3s_{1/2}$	0.507	0.113	$2d_{3/2} - 3s_{1/2}$	1.174	0.025
below proton Fermi level					
$3s_{1/2} - 1h_{9/2}$	4.527	0.094	$3s_{1/2} - 1h_{9/2}$	3.362	0.095
$1h_{9/2} - 2f_{7/2}$	2.455	0.078	$1h_{9/2} - 2f_{7/2}$	3.260	0.081
$2f_{7/2} - 1i_{13/2}$	1.659	0.094	$2f_{7/2} - 1i_{13/2}$	0.626	0.103
$1i_{13/2} - 2f_{5/2}$	0.271	0.128	$1i_{13/2} - 2f_{5/2}$	1.283	0.136
$2f_{5/2} - 3p_{3/2}$	0.799	0.033	$2f_{5/2} - 3p_{3/2}$	1.331	0.031
$3p_{3/2} - 3p_{1/2}$	0.696	0.017	$3p_{3/2} - 3p_{1/2}$	0.695	0.016
below neutron Fermi level					
$3p_{1/2} - 1i_{11/2}$	4.380	0.109	—	—	—
$1i_{11/2} - 2g_{9/2}$	0.827	0.118	—	—	—
$2g_{9/2} - 3d_{5/2}$	1.816	0.022	—	—	—
$3d_{5/2} - 2g_{7/2}$	0.018	0.036	—	—	—
$2g_{7/2} - 4s_{1/2}$	0.256	0.044	—	—	—
$4s_{1/2} - 1j_{15/2}$	0.003	0.084	—	—	—
$1j_{15/2} - 3d_{3/2}$	0.316	0.090	—	—	—
$3d_{3/2} - 4p_{3/2}$	2.837	0.044	—	—	—
$4p_{3/2} - 4p_{1/2}$	0.113	0.003	—	—	—

The detailed analysis of the results of the calculations shows that the freedom to rebalance the depths of the proton and neutron potentials is a major source of these statistical errors in the energies of the single-particle states. Indeed, it was observed that when proton potential becomes deeper as compared with the one in the opti-

imum functional, the neutron potential becomes less deep as compared with the one in optimum functional. This leads to more/less bound proton/neutron single-particle states and allows to keep total energy of the system close to the one in the optimum functional. The opposite situation with deeper neutron and less deep proton potentials takes place with similar frequency.

In general, statistical errors in the absolute energies of the single-particle states could affect model predictions for the position of the two-neutron drip line. Indeed, as discussed in Ref. [28] its position sensitively depends on the positions (in absolute energy) and the distribution of the single-particle states (and especially high- j intruder and extruder ones) located around the continuum limit. However, in the nuclei around ^{266}Pb the standard deviations $\sigma(e_i)$ for such neutron single-particle states are safely below 0.1 MeV (see Table V); the only exception is the $\nu 1j_{13/2}$ orbital for which $\sigma(e_i) = 0.164$ MeV. Thus, it is reasonable to expect that the impact of statistical errors in the energies of the single-particle states on the position of two-neutron drip line will be rather modest. Moreover, these statistical errors are substantially smaller than systematic uncertainties in the predictions of the energies of single-particle states which for many orbitals exceed 1 MeV in nuclei near two-neutron drip line (see Figs. 11c and 6c in Ref. [28]). These facts suggest that the theoretical uncertainties in the prediction of the position of two-neutron drip line are dominated by systematic ones.

While the accuracy of the prediction of the position of the neutron drip line is sensitive to calculated absolute energies of the single-particle states, the accuracy of the reproduction of the single-particle spectra depends mostly on the predictions of the relative energies of the single-particle states. Tables VII, VIII and IX show the mean relative energies $\overline{\Delta e_i}$ of the pairs of neighboring single-particle states (as defined in the NL5(C) functional) and related standard deviations $\sigma(\Delta e_i)$. One can see that in all nuclei the $\sigma(\Delta e_i)$ values are substantially smaller than the $\overline{\Delta e_i}$ values. They are also much smaller than the deviations between theory and experiment for one-(quasi)-particle configurations in spherical [21, 67, 70] and deformed [34, 35] nuclei. Here we assume that statistical errors in the description of the energies of deformed single-particle states are similar to spherical ones which is a reasonable assumption considering that deformed states emerge from spherical ones. Thus, one can conclude that systematic uncertainties in the energies of the single-particle states are more important than statistical ones for the predictions of the single-particle spectra.

The underlying single-particle structure is responsible for the differences in the predictions of the ground state deformations of superheavy nuclei near the $Z = 120$ and $N = 184$ lines (Ref. [29]). These nuclei could be either spherical or oblate dependent on employed CEDF. Thus, it is important to estimate statistical errors in the predictions of the $Z = 120$ and $N = 184$ spherical shell gaps

TABLE VIII. The same as Table VII but for the ^{266}Pb nucleus. The states in the energy range from ~ -42 MeV up to ~ -20 MeV are omitted in order to simplify the table.

Neutron			Proton		
Orbital pairs (m, j)	$\overline{\Delta e_\nu}$	$\sigma(\Delta e_\nu)$	Orbital pairs (m, j)	$\overline{\Delta e_\pi}$	$\sigma(\Delta e_\pi)$
1	2	3	4	5	6
$1s_{1/2} - 1p_{3/2}$	5.123	0.037	$1s_{1/2} - 1p_{3/2}$	4.447	0.031
$1p_{3/2} - 1p_{1/2}$	0.355	0.008	$1p_{3/2} - 1p_{1/2}$	0.428	0.010
—	—	—	—	—	—
$2d_{5/2} - 2d_{3/2}$	1.143	0.029	$2d_{5/2} - 1h_{11/2}$	0.811	0.071
$2d_{3/2} - 3s_{1/2}$	0.807	0.016	$1h_{11/2} - 2d_{3/2}$	0.322	0.096
$3s_{1/2} - 1h_{11/2}$	0.024	0.077	$2d_{3/2} - 3s_{1/2}$	1.348	0.019
			below proton Fermi level		
$1h_{11/2} - 1h_{9/2}$	3.543	0.101	$3s_{1/2} - 1h_{9/2}$	2.001	0.063
$1h_{9/2} - 2f_{7/2}$	2.669	0.055	$1h_{9/2} - 2f_{7/2}$	3.859	0.061
$2f_{7/2} - 2f_{5/2}$	1.502	0.034	$2f_{7/2} - 1i_{13/2}$	0.451	0.079
$2f_{5/2} - 1i_{13/2}$	0.244	0.094	$1i_{13/2} - 2f_{5/2}$	1.043	0.108
$1i_{13/2} - 3p_{3/2}$	0.581	0.088	$2f_{5/2} - 3p_{3/2}$	1.717	0.025
$3p_{3/2} - 3p_{1/2}$	0.562	0.014	$3p_{3/2} - 3p_{1/2}$	0.570	0.014
$3p_{1/2} - 1i_{11/2}$	3.342	0.075	$3p_{1/2} - 1i_{11/2}$	1.307	0.074
$1i_{11/2} - 2g_{9/2}$	1.425	0.084	$1i_{11/2} - 2g_{9/2}$	3.196	0.082
$2g_{9/2} - 2g_{7/2}$	1.590	0.031	$2g_{9/2} - 1j_{15/2}$	0.349	0.079
$2g_{7/2} - 3d_{5/2}$	0.291	0.035	$1j_{15/2} - 2g_{7/2}$	1.338	0.105
$3d_{5/2} - 1j_{15/2}$	0.156	0.085	$2g_{7/2} - 3d_{5/2}$	1.748	0.034
$1j_{15/2} - 4s_{1/2}$	0.349	0.093	$3d_{5/2} - 3d_{3/2}$	0.688	0.014
$4s_{1/2} - 3d_{3/2}$	0.090	0.014	$3d_{3/2} - 4s_{1/2}$	0.590	0.018
			below neutron Fermi level		
$3d_{3/2} - 2h_{11/2}$	4.290	0.015	$4s_{1/2} - 1j_{13/2}$	1.056	0.109
$2h_{11/2} - 4p_{3/2}$	0.255	0.064			
$4p_{3/2} - 1j_{13/2}$	0.113	0.138			
$1j_{13/2} - 4p_{1/2}$	0.054	0.137			
$4p_{1/2} - 3f_{7/2}$	0.086	0.022			
$3f_{7/2} - 3f_{5/2}$	0.452	0.011			
$3f_{5/2} - 2h_{9/2}$	0.389	0.041			

formed between the $\pi 2f_{5/2} - \pi 3p_{3/2}$ and $\nu 4s_{1/2} - \nu 1j_{13/2}$ pairs of the states (see Figs. 1b and 1d in Ref. [29]). These errors are very small ($\sigma(\Delta e_\pi) = 0.030$ MeV) for the $Z = 120$ shell gap which is characterized by the mean size of 2.116 MeV (see Table IX). They are bigger for the $N = 184$ shell gap ($\sigma(\Delta e_\nu) = 0.102$ MeV) the mean size of which is equal to 1.177 MeV (Table IX). These statistical errors are substantially smaller than the systematic uncertainties in the shell gap sizes (see Fig. 2a in Ref. [29]) which, as a result, are almost fully responsible for the differences in the predictions of the ground state properties of the superheavy nuclei under discussion.

The results presented in Tables VII, VIII, and IX provide also the information on statistical errors in the description of spin-orbit splittings. Indeed, these tables contain the pairs of the orbitals which form spin-orbit doublets such as $p_{3/2} - p_{1/2}$, $d_{5/2} - d_{3/2}$, $f_{7/2} - f_{5/2}$, $g_{9/2} - g_{7/2}$ and $h_{11/2} - h_{9/2}$. For the majority of the spin-orbit doublets standard deviations $\sigma(\Delta e_i(m, j))$ are of the order of 2.7% of their mean splitting energies $\Delta e_i(m, j)$. Indeed, for 14 spin-orbit doublets of ^{208}Pb seen in Table VII, the ratio $\sigma(\Delta e_i(m, j))/\Delta e_i(m, j)$ is

TABLE IX. The same as Table VII but for the $^{304}120$ nucleus. Neutron states in the energy range from ~ -50 MeV up to ~ -25 MeV and proton states in the energy range from ~ -35 MeV up to ~ -12 MeV are omitted in order to simplify the table.

Neutron			Proton		
Orbital pairs (m, j)	$\overline{\Delta e_\nu}$	$\sigma(\Delta e_\nu)$	Orbital pairs (m, j)	$\overline{\Delta e_\pi}$	$\sigma(\Delta e_\pi)$
1	2	3	4	5	6
$1s_{1/2} - 1p_{3/2}$	4.050	0.025	$1s_{1/2} - 1p_{3/2}$	3.935	0.020
$1p_{3/2} - 1p_{1/2}$	0.239	0.004	$1p_{3/2} - 1p_{1/2}$	0.299	0.006
—	—	—	—	—	—
$3s_{1/2} - 1h_{9/2}$	1.106	0.026	$3s_{1/2} - 1h_{9/2}$	1.180	0.032
$1h_{9/2} - 2f_{7/2}$	3.863	0.044	$1h_{9/2} - 1i_{13/2}$	4.019	0.070
$2f_{7/2} - 1i_{13/2}$	0.559	0.072	$1i_{13/2} - 2f_{7/2}$	0.247	0.082
$1i_{13/2} - 2f_{5/2}$	0.941	0.105	$2f_{7/2} - 2f_{5/2}$	1.486	0.035
			below proton Fermi level		
$2f_{5/2} - 3p_{3/2}$	2.660	0.022	$2f_{5/2} - 3p_{3/2}$	2.116	0.030
$3p_{3/2} - 3p_{1/2}$	0.346	0.006	$3p_{3/2} - 3p_{1/2}$	0.318	0.006
$3p_{1/2} - 1i_{11/2}$	0.659	0.058	$3p_{1/2} - 1i_{11/2}$	0.595	0.058
$1i_{11/2} - 2g_{9/2}$	3.094	0.075	$1i_{11/2} - 1j_{15/2}$	3.146	0.109
$2g_{9/2} - 1j_{15/2}$	0.385	0.083	$1j_{15/2} - 2g_{9/2}$	0.473	0.090
$1j_{15/2} - 2g_{7/2}$	1.603	0.123	$2g_{9/2} - 2g_{7/2}$	1.946	0.045
$2g_{7/2} - 3d_{5/2}$	1.870	0.020			
$3d_{5/2} - 3d_{3/2}$	0.322	0.005			
$3d_{3/2} - 4s_{1/2}$	0.642	0.011			
below neutron Fermi level					
$4s_{1/2} - 1j_{13/2}$	1.177	0.102			
$1j_{13/2} - 2h_{11/2}$	1.917	0.107			
$2h_{11/2} - 1k_{17/2}$	0.609	0.082			
$1k_{17/2} - 2h_{9/2}$	1.442	0.113			
$2h_{9/2} - 3f_{7/2}$	0.600	0.041			
$3f_{7/2} - 3f_{5/2}$	0.438	0.004			
$3f_{5/2} - 4p_{3/2}$	0.269	0.020			
$4p_{3/2} - 4p_{1/2}$	0.179	0.003			
$4p_{1/2} - 5s_{1/2}$	2.094	0.037			
$5s_{1/2} - 4d_{5/2}$	0.468	0.003			
$4d_{5/2} - 4d_{3/2}$	0.039	0.001			

located in the range from 0.023 up to 0.031. In ^{266}Pb and $^{304}120$ nuclei, the standard deviations $\sigma(\Delta e_i(m, j))$ are of the order of 2.4% and 2.0% of their mean splitting energies $\Delta e_i(m, j)$, respectively (see Tables VIII and IX). Thus, statistical errors (as compared with those seen in ^{208}Pb) in the description of spin-orbit splittings do not increase on going towards the extremes of neutron number or charge.

Statistical errors in the description of the single-particle energies have also been analysed in lighter ^{48}Ca and ^{132}Sn nuclei. They show the same general features as those discussed above in $^{208,266}\text{Pb}$ and $^{304}120$. As compared with ^{208}Pb , statistical errors in the energies of the single-particle states located in the vicinity of the Fermi levels are similar/somewhat smaller in $^{132}\text{Sn}/^{48}\text{Ca}$.

It is interesting to compare our CDFT results with those obtained in Skyrme DFT framework with the UNEDF0 functional and presented in Table I of Ref. [6]. For the neutron/proton states of ^{208}Pb shown in this table the statistical errors obtained in the Skyrme DFT cal-

culations are on average by a factor of 2.05/1.46 larger than those obtained in our CDFT calculations (compare Table IV in the present manuscript with Table I of Ref. [6]). In addition, there is one principal difference between the CDFT and Skyrme DFT results. The standard deviations $\sigma(\Delta e_i(m, j))$ for the spin-orbit splittings are very small in the CDFT calculations; they are typically on the level of 2-3% of total size of spin-orbit splitting. On the contrary, they are substantially larger (both in relative and absolute senses) in the Skyrme DFT calculations (see Table I in Ref. [6]).

VII. CONCLUSIONS

Statistical errors in ground state observables and single-particle properties of spherical even-even nuclei and their propagation to the limits of nuclear landscape have been investigated in covariant density functional theory for the first time. The main results can be summarized as follows:

- Statistical errors in binding energies, charge radii, neutron skins and two-neutron separation energies have been studied for the Ca, Ni, Sn and Pb nuclei located between two-proton and two-neutron drip lines. While statistical errors for binding energies and neutron skins drastically increase on approaching two-neutron drip line, such a trend does not exist for statistical errors in charge radii and two-neutron separation energies. The latter is contrary to the trends seen in Skyrme density functional theory. Statistical errors obtained in the CDFT calculations are substantially smaller than related systematic uncertainties.
- The absolute energies of the single-particle states in the vicinity of the Fermi level are characterized by low statistical errors ($\sigma(e_i) \sim 0.1$ MeV). This is also true for relative energies of the single-particle states. These statistical errors are substantially smaller than systematic uncertainties in the predictions of the absolute and relative energies of the single-particle states. Thus, they are not expected to modify in a substantial way the predictions of a given CEDF. This is true both for known nuclei and for nuclear extremes such as the vicinity of neutron-drip line and the region of superheavy elements.
- The statistical errors in the predictions of spin-orbit splittings are rather small. For the spin-orbit doublets in studied nuclei, the standard deviations $\sigma(\Delta e_i(m, j))$ are of the order of 2.4% of their mean splitting energies $\overline{\Delta e_i(m, j)}$. These errors are quite robust and they do not increase on going towards the extremes of neutron number or charge.
- Statistical errors in the description of physical observables related to the ground state and single-

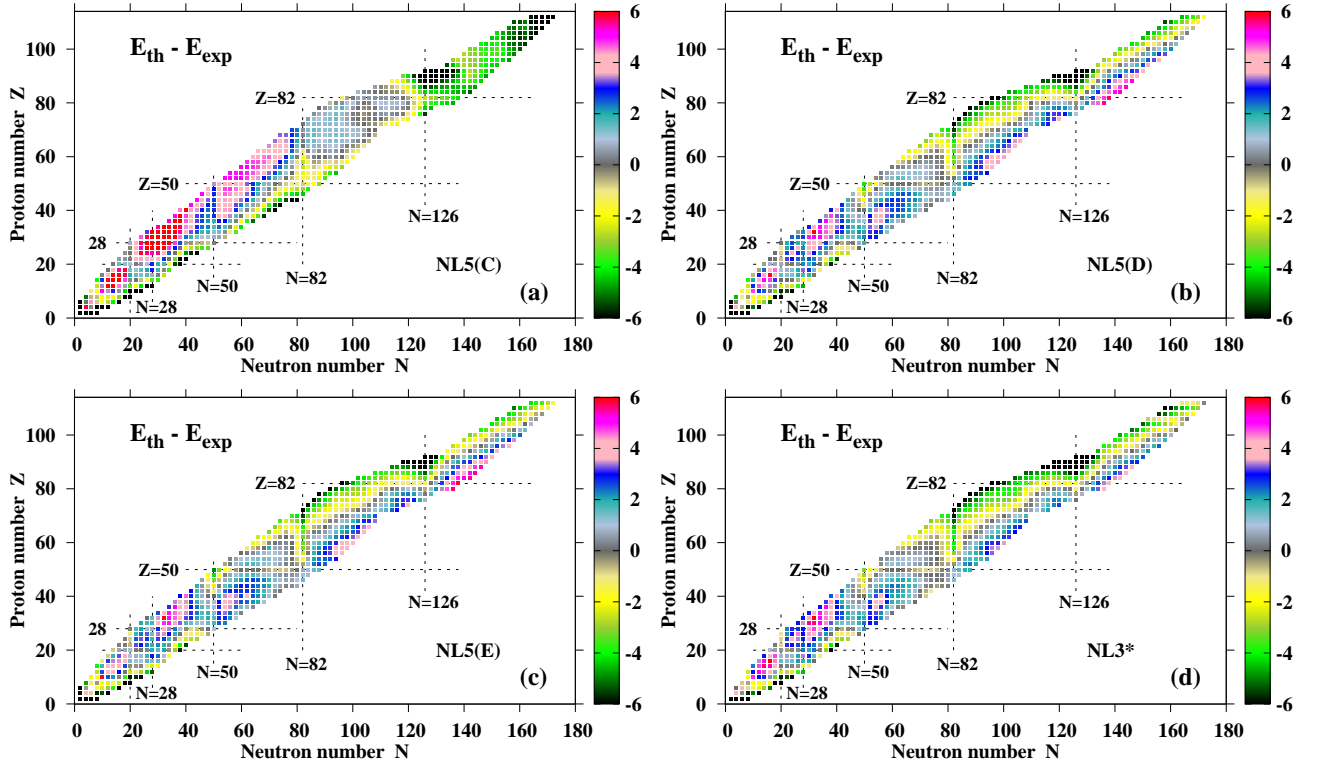


FIG. 9. (Color online) The differences $E_{th} - E_{exp}$ between calculated and experimental binding energies for the indicated CEDFs. The experimental data are taken from Ref. [72] and 830 even-even nuclei, for which measured and estimated masses are available, are included. If $E_{th} - E_{exp} < 0$, the nucleus is more bound in the calculations than in experiment.

particle degrees of freedom are substantially lower in CDFT as compared with Skyrme DFT. A special feature of CDFT due to which the parameters of the ω and σ mesons, defining the basis features of the nucleus such as a nucleonic potential, are well localized in very narrow range of the parameter hyperspace, is responsible for that. Note that fixing the g_ρ , g_2 and g_3 parameters of the model leads to drastic reduction of statistical errors as compared with the case when all parameters of the non-linear functional are permitted to vary in Monte-Carlo procedure.

- The present investigation reveals strong correlations between a number of the parameters defining the non-linear CEDFs. Note that these correlations are dependent on the details of fitting protocol. They are especially pronounced for the g_2 and g_3 parameters responsible for the density dependence of the model. This suggests that these parameters are not independent. Thus, the accounting of these parametric correlations will allow in future to reduce the number of free parameters of non-linear meson coupling models from six to five.

Considering the structure of non-linear meson coupling models and typical features of existing non-linear CEDFs and their fitting protocols, it is reasonable to expect that

different non-linear functionals will provide comparable statistical errors for the physical observables of interest. This was illustrated by comparison of the results for the NL5(C) and NL5(A) functionals.

Note that obtained statistical errors represent in a sense their upper limit since the fitting protocol includes only limited set of nuclei and empirical data. It is expected that the increase of the size of the dataset in the fitting protocol will lead to further reduction of statistical errors [2].

There are clearly many physical observables which are left outside the present study. However, based on the present results we can evaluate statistical errors of some of them. One of the examples is the energies of the single-particle states in deformed nuclei. The wavefunctions of the deformed single-particle states are the mixtures of the contributions coming from different spherical single-particle states. Thus, the statistical errors for the energies of deformed single-particle states are expected to be of similar magnitude as those for spherical states. However, the fluctuations in their magnitudes are expected to be smaller as compared with spherical states because of the above mentioned mixing. For the same reasons, the statistical errors in charge radii and neutron skins of deformed nuclei are expected to be comparable with spherical ones.

Another example is time-odd mean fields. They have

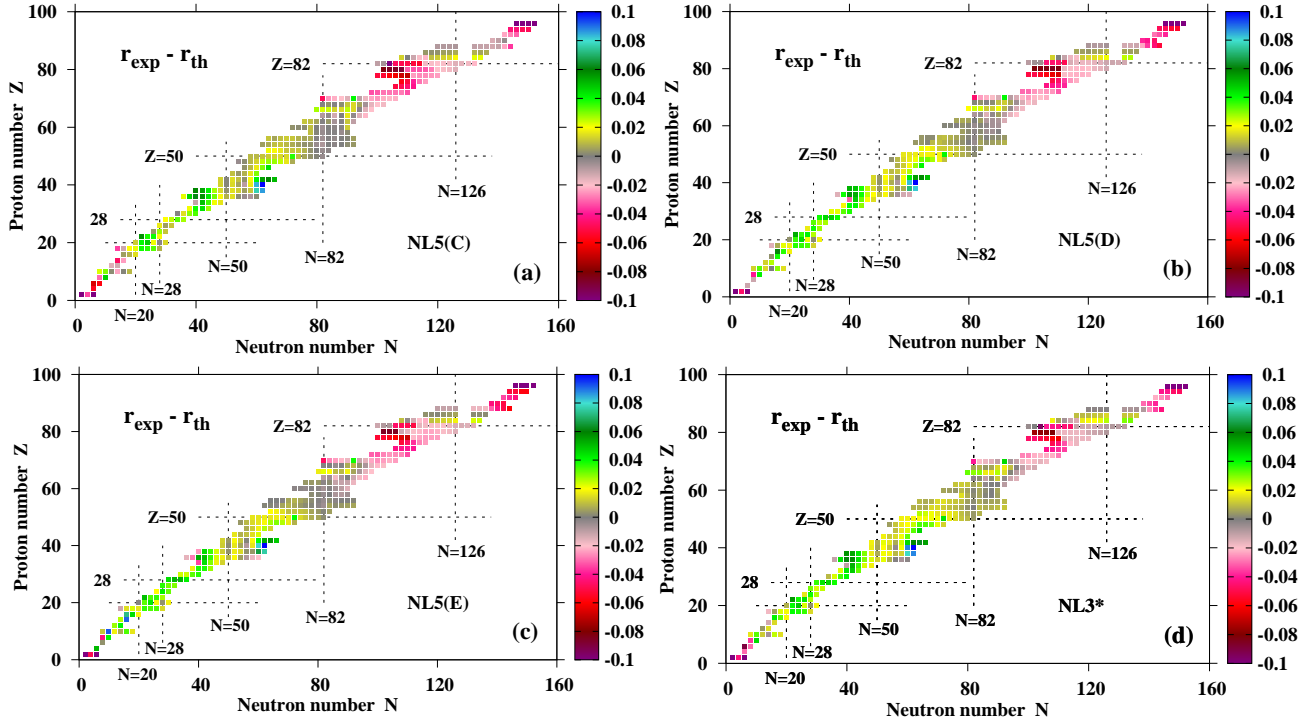


FIG. 10. (Color online) The difference between measured and calculated charge radii r_{ch} for indicated functionals. The experimental data are taken from Ref. [73].

an impact on a considerable number of physical observables in the systems with broken time-reversal symmetries [15, 24]. However, their impact depends on the g_ω and m_ω parameters [24, 71], which according to our results vary very little (see Fig. 2a, b, c, 5b and 6b). Note that m_ω is fixed in many functionals. These facts suggest that statistical errors in time-odd mean fields and the components of physical observables related to time-odd mean fields (such as the contribution to the moment of inertia due to time-odd mean fields [71] or additional binding due to nuclear magnetism [24]) should be reasonably small.

VIII. ACKNOWLEDGMENTS

This material is based upon work supported by the U.S. Department of Energy, Office of Science, Office of Nuclear Physics under Award No. de-sc0013037.

Appendix A: Global performance of the NL5(*) covariant energy density functionals

The global performance of the NL5(C), NL5(D) and NL5(E) functionals in the description of ground state properties of even-even nuclei is presented in Figs. 9 and 10 and summarized in Table X. Experimental data on binding energies of 835 even-even nuclei is taken from Ref. [72]; note that there are 640 measured and 195 esti-

mated masses of even-even nuclei in the AME2012 mass evaluation⁵. Experimental data on charge radii of 351 even-even nuclei is taken from Ref. [73]. The global performance of the NL5(*) functionals is also compared with the one of the NL3* functional studied in details in Refs. [3, 29, 31]. Note that the NL3* is the state-of-the-art functional for the non-linear coupling meson exchange models (see Ref. [3]) with well documented record of successful applications to the ground state properties of even-even nuclei [3, 17, 31], octupole deformation in the ground states of even-even nuclei [30], giant resonances [17], the energies and spectroscopic factors of dominant components of single-particle states in odd-mass nuclei [21, 67], rotating nuclei [17, 36], fission barriers [74, 75], superheavy nuclei [29] etc.

The rms deviations $\Delta E_{rms} \sim 3.7$ MeV between calculated and experimental binding energies E for the NL5(C) CEDF are very similar to those obtained with original NL3 functional (see Ref. [76]). The NL3* functional [3, 17] with $\Delta E_{rms} = 3.0$ MeV represents an improved version of this functional. The NL5(D) and espe-

⁵ For simplicity, we exclude 5 superheavy nuclei with $Z = 114, 116$ and 118 from comparison between theory and experiment since the definition of the ground state (prolate normal deformed or superdeformed) in these nuclei requires extensive and time consuming calculations in the axial RHB code with octupole deformation and triaxial RHB code. However, the exclusion of these nuclei has very little effect on rms deviations presented in the columns 2-5 of Table X.

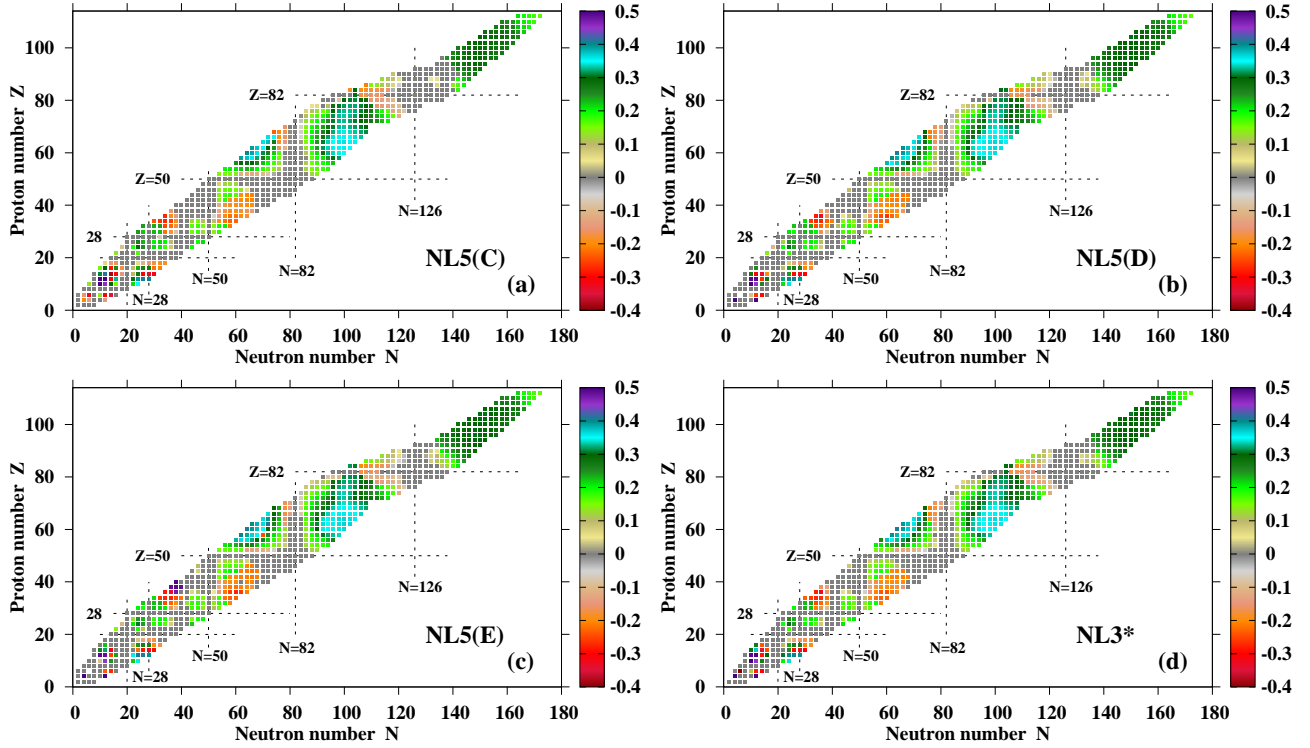


FIG. 11. (Color online) Charge quadrupole deformations β_2 of the ground states in even-even nuclei obtained in the RHB calculations with indicated CEDFs.

cially NL5(E) functionals provide further improvement of global description of masses as compared with the NL3* one (see Table X). They produce comparable with NL3* description of two-neutron (S_{2n}) and two-proton (S_{2p}) separation energies (see Table X). With minor differences the distribution of the $E_{th} - E_{exp}$ quantities in the (Z, N) plane is similar for the NL5(D), NL5(E) and NL3* functionals (Fig. 9). On the contrary, there are substantial differences between the NL5(C) and NL3* functionals in that respect.

All functionals give comparable rms deviations for charge radii $\Delta(r_{ch})_{rms}$ (see Table X). Note that the last column in Table X excludes experimental data on He ($Z = 2$) (3 data points) and Cm ($Z = 96$) (4 data points) nuclei (see detailed motivation in Sect. X of Ref. [3]). It is clear that DFTs cannot describe very light nuclei such as He. In addition, experimental charge radii of the Cm ($Z = 96$) nuclei are lower than those of Pu ($Z = 94$) and U ($Z = 92$) [73]. Such feature goes against a general trend of the increase of charge radii with the increase of proton number for comparable deformations and could be described neither in CDFT (see Ref. [3]) nor in non-relativistic DFT calculations with Gogny D1S functional (see Supplemental Material to Ref. [77]).

Appendix B: The examples of the spread of the parameters in non-relativistic functionals

Tables XI and XII illustrate the spread of model parameters in the Gogny and Skyrme energy density functionals. These are state-of-the-art finite range Gogny functionals D1S [78] and D1M [79] and state-of-the-art zero-range Skyrme functionals UNEDF0 [81], UNEDF1[82], BSk28 [83] and BSk29 [83]. They are compared with older Skyrme functionals SLy4 [84] and SkM* [85] and first Gogny functional D1 [80]. Apart of D1, all other functionals are still in extensive use.

D1 [80] is the first Gogny functional. However, it was found in Ref. [86] that it does not reproduce fission barriers in actinides. Thus, the D1S functional was fitted in Ref. [86]: fitting protocol of this functional includes experimental data on fission barriers in addition to the data used in the fitting protocol of the D1 functional. One can see in Table XI that for the same radial ranges μ_i of the D1 and D1S forces, the absolute values of the strength parameters W_i , B_i , H_i and M_i of the central force of D1S differ by almost an order of magnitude from those of D1. In addition, the strength W_{LS} of the spin-orbit interaction has different signs in these two functionals. The D1S functional has been successfully applied to the description of many nuclear phenomena [14] and it is still widely used by many practitioners of the Gogny DFT. The D1M functional has been fitted globally to nuclear masses in Ref. [79]. Shorter ranges of interaction are used in it (see

TABLE X. The rms deviations ΔE_{rms} , $\Delta(S_{2n})_{rms}$ ($\Delta(S_{2p})_{rms}$) and $\Delta(r_{ch})_{rms}$ between calculated and experimental binding energies E , two-neutron (-proton) separation energies S_{2n} (S_{2p}) and charge radii r_{ch} for indicated CEDFs. For first three observables, they are given with respect of "measured" (640 nuclei) and "measured+estimated" (830 nuclei) sets of experimental masses. For the calculations of the $\Delta(r_{ch})_{rms}$ values, all experimental data are used in column 6, while the data on radii of He ($Z = 2$) and Cm ($Z = 96$) isotopes are excluded in column 7. See text for the discussion of these cases.

CEDF	measured	measured+estimated			charge radii	
	ΔE_{rms} [MeV]	ΔE_{rms} [MeV]	$\Delta(S_{2n})_{rms}$ [MeV]	$\Delta(S_{2p})_{rms}$ [MeV]	$\Delta(r_{ch})_{rms}$ [fm]	$\Delta(r_{ch})_{rms}$ [fm]
1	2	3	4	5	6	7
NL5(C)	3.41	3.71	1.37	1.54	0.040	0.0284
NL5(D)	2.83	2.90	1.22	1.29	0.041	0.0277
NL5(E)	2.73	2.81	1.23	1.29	0.042	0.0288
NL3*	2.96	3.00	1.23	1.29	0.041	0.0283

TABLE XI. The values of the parameters of different sets for the finite range Gogny forces (see equations in the appendix of Ref. [78] or Eq. (3) in Ref. [79] for the definition of the Gogny force). The μ_i ($i = 1, 2$) parameters describe the range of the interaction. The strength of the Wigner, Bartlett, Heisenberg and Majorana terms is given by W_i , B_i , H_i and M_i , respectively. The parameters t_0 , x_0 and α define the density dependence of the interaction, while W_{LS} zero-range two-body spin-orbit interaction.

Parameters	D1S[78]		D1[80]		D1M[79]	
μ_i (fm)	0.7	1.2	0.7	1.2	0.5	1.0
W_i [MeV]	-1720.30	103.64	-402.4	-21.30	-12797.57	490.95
B_i [MeV]	1300.00	-163.48	-100.0	-11.77	14048.85	-752.27
H_i [MeV]	-1813.53	162.81	-496.2	37.27	-15144.43	675.12
M_i [MeV]	1397.60	-223.93	-23.56	-68.81	11963.89	-693.57
t_0 [MeV]	1390.6		1350.0		1562.22	
x_0	1		1		1	
α	1/3		1/3		1/3	
W_{LS} [MeV]	-130.0		115.0		115.56	

TABLE XII. The values of the parameters for different Skyrme forces. When needed the parameters are reduced to the form of the Skyrme force employed for the BSk class of the functionals (see Eq. (1) in Ref. [88]). The parameters t_0 and x_0 define the central term. t_1 , x_1 , t_2 , x_2 are the parameters of the non-local terms. Density dependence is defined by t_3 , x_3 and γ parameters. The W_0 and W_1 parameters define the spin-orbit interaction. The BSk28 and BSk29 functionals have many additional parameters as compared with other functionals; some of them (t_4 , x_4 , t_5 , x_5) are shown here but others (see 9 bottom lines of Table 1 in Ref. [83]) are omitted for simplicity.

Parameters	UNEDF0 [81]	UNEDF1 [82]	SLy4 [84]	SKM* [85]	BSk28 [83]	BSk29 [83]
t_0 [MeV fm ³]	-1883.68781034	-2078.32802326	-2488.91	-2645.00	-3988.86	-3970.40
t_1 [MeV fm ⁵]	277.50021224	239.40081204	486.82	410.00	395.769	394.880
t_2 [MeV fm ⁵]	608.43090559	1575.11954190	-546.39	-135.00		
t_3 [MeV fm ^{3+3α}]	13901.94834463	14263.64624708	13777.0	15595.0	22774.4	22649.3
t_4 [MeV fm ^{5+3β}]					-100.000	-100.000
t_5 [MeV fm ^{5+3γ}]					-150.000	-150.000
x_0	0.00974375	0.05375692	0.834	0.09	0.928026	0.964850
x_1	-1.77784395	-5.07723238	-0.344	0.00	0.0274980	-0.0047741
x_2	-1.67699035	-1.36650561	-1.000	0.00		
$t_2 x_2$ [MeV fm ⁵]					-1388.61	-1388.95
x_3	-0.38079041	-0.16249117	1.354	0.00	1.09482	1.14453
x_4					2.0000	2.00000
x_5					-11.0000	-11.0000
W_0 [MeV fm ⁵]	33.9006	109.6845943	123.0	130.0	80.489	64.600
W_1 [MeV fm ⁵]					180.411	0
α	0.32195599	0.27001801	1/6	1/6	1/12	1/12
β					1/2	1/2
γ					1/12	1/12
ν					1	0
y_ω					0	2

Table XI); as a result, the strengths of the central force terms change (as compared with D1S) by approximately one order of magnitude for $i = 1$ and by a factor of approximately 4 for $i = 2$. As compared with D1S, the t_0 strength is modified by more than 10% but the strength of spin-orbit interaction remains unchanged.

Contrary to the Gogny functionals there is significant number of Skyrme energy density functionals (SEDF); the compilation of Ref. [87] reveals 240 SEDFs developed by 2012. However, one should recognize that only small subset of these functionals is used in the calculations of finite nuclei in a repetitive manner. Table XII lists some of them. As compared with Gogny functionals shown in Table XII, the variations in the parameters of SEDF (see Table XII) are less drastic. However, even the parameters of recent classes of the SEDF, namely UNEDF* [81, 82] and BSk* [83], differ substantially. This reflects the differences in the form of SEDFs and the details of the fitting protocols; see also Sect. 5.C. of Ref. [12] for short

review of fitting protocols employed in nuclear DFTs.

These results clearly show the difference between relativistic and non-relativistic DFTs. In CDFT, the parameters of the σ - and ω -mesons are well localized for all functionals (see Fig. 2) independent of the form of the density dependence, the properties of the ρ -meson or the details of the fitting protocol. Basically starting from first successful CEDF NL1 [46], fitted 33 years ago, the parameters of the σ - and ω -mesons of all successful functionals developed over the years and quoted in the present manuscript are very close to each other (see Fig. 2). This is due to the fact that nucleonic potential in CDFT is build as a sum of large attractive scalar potential (related to σ -meson) and large repulsive vector potential (related to ω -meson) which limits possible range of the variations of the parameters. On the contrary, as illustrated in Tables XI and XII the level of the localization of the parameters is lower (and the spread of the parameters is higher) in non-relativistic functionals.

-
- [1] P. G. Reinhard and W. Nazarewicz, Phys. Rev. C **81**, 051303(R) (2010).
- [2] J. Dobaczewski, W. Nazarewicz, and P.-G. Reinhard, J. Phys. G **41**, 074001 (2014).
- [3] S. E. Agbemava, A. V. Afanasjev, D. Ray, and P. Ring, Phys. Rev. C **89**, 054320 (2014).
- [4] J. Erler, N. Birge, M. Kortelainen, W. Nazarewicz, E. Olsen, A. M. Perhac, and M. Stoitsov, Nature **486**, 509 (2012).
- [5] A. V. Afanasjev, S. E. Agbemava, D. Ray, and P. Ring, Phys. Lett. B **726**, 680 (2013).
- [6] Y. Gao, J. Dobaczewski, M. Kortelainen, J. Toivanen, and D. Tarpanov, Phys. Rev. C **87**, 034324 (2013).
- [7] J. D. McDonnell, N. Schunck, D. Higdon, J. Sarich, S. M. Wild, and W. Nazarewicz, Phys. Rev. Lett. **114**, 122501 (2015).
- [8] D. Martin, A. Arcones, W. Nazarewicz, and E. Olsen, Phys. Rev. Lett. **116**, 121101 (2016).
- [9] M. R. Mumpower, R. Surman, G. C. McLaughlin, and A. Aprahamian, Prog. Part. Nucl. Phys. **86**, 86 (2016).
- [10] A. E. Lovell, F. M. Nunes, J. Sarich, and S. M. Wild, Phys. Rev. C **95**, 024611 (2017).
- [11] S. Brandt, *Data analysis. Statistical and Computational Methods for Scientists and Engineers*. (Springer International Publishing, Switzerland, 2014).
- [12] M. Bender, P.-H. Heenen, and P.-G. Reinhard, Rev. Mod. Phys. **75**, 121 (2003).
- [13] J. Boguta and R. Bodmer, Nucl. Phys. **A292**, 413 (1977).
- [14] S. Peru and M. Martini, Eur. Phys. J **50**, 88 (2014).
- [15] D. Vretenar, A. V. Afanasjev, G. A. Lalazissis, and P. Ring, Phys. Rep. **409**, 101 (2005).
- [16] G. A. Lalazissis, T. Nikšić, D. Vretenar, and P. Ring, Phys. Rev. C **71**, 024312 (2005).
- [17] G. A. Lalazissis, S. Karatzikos, R. Fossion, D. P. Arteaga, A. V. Afanasjev, and P. Ring, Phys. Lett. **B671**, 36 (2009).
- [18] T. Nikšić, D. Vretenar, and P. Ring, Phys. Rev. C **78**, 034318 (2008).
- [19] S. Typel and H. H. Wolter, Nucl. Phys. **A656**, 331 (1999).
- [20] Extended Density Functionals in Nuclear Structure Physics, *Lecture Notes in Physics*, edited by G. A. Lalazissis, P. Ring, and D. Vretenar (Springer-Verlag, Heidelberg, 2004) **Vol. 641** (2004).
- [21] E. V. Litvinova and A. V. Afanasjev, Phys. Rev. C **84**, 014305 (2011).
- [22] T. D. Cohen, R. J. Furnstahl, and K. Griegel, Phys. Rev. C **45**, 1881 (1992).
- [23] W. Koepf and P. Ring, Nucl. Phys. A **493**, 61 (1989).
- [24] A. V. Afanasjev and H. Abusara, Phys. Rev. C **81**, 014309 (2010).
- [25] J. Meng, H. Toki, S. G. Zhou, S. Q. Zhang, W. H. Long, and L. S. Geng, Prog. Part. Nucl. Phys. **57**, 470 (2006).
- [26] T. Nikšić, D. Vretenar, and P. Ring, Prog. Part. Nucl. Phys. **66**, 519 (2011).
- [27] "Relativistic Density Functional for Nuclear Structure", (World Scientific Publishing Co), Edited by Jie Meng, Int. Rev. Nucl. Phys. **10** (2016).
- [28] A. V. Afanasjev, S. E. Agbemava, D. Ray, and P. Ring, Phys. Rev. C **91**, 014324 (2015).
- [29] S. E. Agbemava, A. V. Afanasjev, T. Nakatsukasa, and P. Ring, Phys. Rev. C **92**, 054310 (2015).
- [30] S. E. Agbemava, A. V. Afanasjev, and P. Ring, Phys. Rev. C **93**, 044304 (2016).
- [31] A. V. Afanasjev and S. E. Agbemava, Phys. Rev. C **93**, 054310 (2016).
- [32] S. E. Agbemava and A. V. Afanasjev, Phys. Rev. C **96**, 024301 (2017).
- [33] S. E. Agbemava, A. V. Afanasjev, D. Ray, and P. Ring, PRC **95** (2017).
- [34] A. V. Afanasjev and S. Shawaqfeh, Phys. Lett. B **706**, 177 (2011).
- [35] J. Dobaczewski, A. V. Afanasjev, M. Bender, L. M. Robledo, and Y. Shi, Nucl. Phys. A **944**, 388 (2015).
- [36] A. V. Afanasjev and O. Abdurazakov, Phys. Rev. C **88**, 014320 (2013).
- [37] I. Debes and J. Dudek, Acta Phys. Polonica **B10**, 51 (2017).

- [38] T. Nikšić, N. Paar, P.-G. Reinhard, and D. Vretenar, *J. Phys. G* **42**, 034008 (2015).
- [39] T. Haverinen and M. Kortelainen, *J. Phys. G* **44**, 044008 (2017).
- [40] T. Bürvenich, D. Madland, and P.-G. Reinhard, *Nucl. Phys. A* **744**, 92 (2004).
- [41] R. T. Birge, *Phys. Rev.* **40**, 207 (1932).
- [42] B. D. Serot and J. D. Walecka, *Adv. Nucl. Phys.* **16**, 1 (1986).
- [43] Y. K. Gambhir, P. Ring, and A. Thimet, *Ann. Phys. (N.Y.)* **198**, 132 (1990).
- [44] W. Kohn and L. J. Sham, *Phys. Rev.* **137**, A1697 (1965).
- [45] Y. Tian, Z. Y. Ma, and P. Ring, *Phys. Lett. B* **676**, 44 (2009).
- [46] P.-G. Reinhard, M. Rufa, J. Maruhn, W. Greiner, and J. Friedrich, *Z. Phys. A* **323**, 13 (1986).
- [47] M. Rufa, P.-G. Reinhard, J. A. Maruhn, W. Greiner, and M. R. Strayer, *Phys. Rev. C* **38**, 390 (1988).
- [48] M. Sharma, M. Nagarajan, and P. Ring, *Phys. Lett. B* **312**, 377 (1993).
- [49] G. A. Lalazissis, J. König, and P. Ring, *Phys. Rev. C* **55**, 540 (1997).
- [50] M. Dutra, O. Lourenco, S. S. Avancini, B. V. Carlson, A. Delfino, D. P. Menezes, C. Providencia, S. Typel, and J. R. Stone, *Phys. Rev. C* **90**, 055203 (2014).
- [51] S. Abrahamyan *et al.*, *Phys. Rev. Lett.* **108**, 112502 (2012).
- [52] The PREX-II proposal, unpublished, available at hallaweb.jlab.org/parity/prex.
- [53] A. Krasznahorkay, M. Fujiwara, P. van Aarle, H. Akimune, I. Daito, H. Fujimura, Y. Fujita, M. N. Harakeh, T. Inomata, J. Jänecke, S. Nakayama, A. Tamii, M. Tanaka, H. Toyokawa, W. Uijen, and M. Yosoi, *Phys. Rev. Lett.* **82**, 3216 (1999).
- [54] K. Yako, H. Sagawa, and H. Sakai, *Phys. Rev. C* **74**, 051303 (2006).
- [55] C. M. Tarbert, D. P. Watts, D. I. Glazier, P. Aguar, J. Ahrens, J. R. M. Annand, H. J. Arends, R. Beck, V. Bekrenev, B. Boillat, A. Braghieri, D. Branford, W. J. Briscoe, J. Brudvik, S. Cherepnaya, R. Codling, E. J. Downie, K. Foehl, P. Grabmayr, R. Gregor, E. Heid, D. Hornidge, O. Jahn, V. L. Kashevarov, A. Knezevic, R. Kondratiev, M. Korolija, M. Kotulla, D. Krambrich, B. Krusche, M. Lang, V. Lisin, K. Livingston, S. Lugert, I. J. D. MacGregor, D. M. Manley, M. Martinez, J. C. McGeorge, D. Mekterovic, V. Metag, B. M. K. Nefkens, A. Nikolaev, R. Novotny, R. O. Owens, P. Pedroni, A. Polonski, S. N. Prakhov, J. W. Price, G. Rosner, M. Rost, T. Rostomyan, S. Schadmand, S. Schumann, D. Sober, A. Starostin, I. Supek, A. Thomas, M. Unverzagt, T. Walcher, L. Zana, and F. Zehr (Crystal Ball at MAMI and A2 Collaboration), *Phys. Rev. Lett.* **112**, 242502 (2014).
- [56] P.-G. Reinhard, *Rep. Prog. Phys.* **52**, 439 (1989).
- [57] P. Ring, *Prog. Part. Nucl. Phys.* **37** (1996).
- [58] M. Bender, K. Rutz, P.-G. Reinhard, J. A. Maruhn, and W. Greiner, *Phys. Rev. C* **60**, 034304 (1999).
- [59] M. Rashdan, *Phys. Rev. C* **63**, 044303 (2001).
- [60] W. Long, J. Meng, N. V. Giai, and S.-G. Zhou, *Phys. Rev. C* **69**, 034319 (2004).
- [61] Z. Ren and H. Toki, *Nucl. Phys. A* **689**, 691 (2001).
- [62] Y. Sugahara and H. Toki, *Nucl. Phys. A* **579**, 557 (1994).
- [63] T. Nikšić, D. Vretenar, P. Finelli, and P. Ring, *Phys. Rev. C* **66**, 024306 (2002).
- [64] X. Roca-Maza, X. Viñas, M. Centelles, P. Ring, and P. Schuck, *Phys. Rev. C* **84**, 054309 (2011).
- [65] T. Nikšić, M. Imbrišak, and D. Vretenar, *Phys. Rev. C* **95**, 054304 (2017).
- [66] M. Kortelainen, J. Erler, W. Nazarewicz, N. Birge, Y. Gao, and E. Olsen, *Phys. Rev. C* **88**, 031305(R) (2013).
- [67] A. V. Afanasjev and E. Litvinova, *Phys. Rev. C* **92**, 044317 (2015).
- [68] M. Bender, W. Nazarewicz, and P.-G. Reinhard, *Phys. Lett. B* **515**, 42 (2001).
- [69] A. V. Afanasjev, T. L. Khoo, S. Frauendorf, G. A. Lalazissis, and I. Ahmad, *Phys. Rev. C* **67**, 024309 (2003).
- [70] A. V. Afanasjev, *J. Phys. G* **42**, 034002 (2015).
- [71] A. V. Afanasjev and H. Abusara, *Phys. Rev. C* **82**, 034329 (2010).
- [72] M. Wang, G. Audi, A. H. Wapstra, F. G. Kondev, M. MacCormick, X. Xu, and B. Pfeiffer, *Chinese Physics* **C36**, 1603 (2012).
- [73] I. Angeli and K. P. Marinova, *At. Data Nucl. Data Tables* **99**, 69 (2013).
- [74] H. Abusara, A. V. Afanasjev, and P. Ring, *Phys. Rev. C* **82**, 044303 (2010).
- [75] H. Abusara, A. V. Afanasjev, and P. Ring, *Phys. Rev. C* **85**, 024314 (2012).
- [76] G. A. Lalazissis, S. Raman, and P. Ring, *At. Data Nucl. Data Table* **71**, 1 (1999).
- [77] J.-P. Delaroche, M. Girod, J. Libert, H. Goutte, S. Hilaire, S. Peru, N. Pillet, and G. F. Bertsch, .
- [78] J. F. Berger, M. Girod, and D. Gogny, *Comp. Phys. Comm.* **63**, 365 (1991).
- [79] S. Goriely, S. Hilaire, M. Girod, and S. Péru, *Phys. Rev. Lett.* **102**, 242501 (2009).
- [80] D. Gogny, in: G. Ripka, M. Porneuf (Eds.), *Nuclear Self-Consistent Fields*, Proc. Internat. Conf. held at the Center for Theoretical Physics, Trieste, Italy, 1975, North-Holland, Amsterdam, , 333 (1975).
- [81] M. Kortelainen, T. Lesinski, J. Moré, W. Nazarewicz, J. Sarich, N. Schunck, M. V. Stoitsov, and S. Wild, *Phys. Rev. C* **82**, 024313 (2010).
- [82] M. Kortelainen, J. McDonnell, W. Nazarewicz, P.-G. Reinhard, J. Sarich, N. Schunck, M. V. Stoitsov, and S. M. Wild, *Phys. Rev. C* **85**, 024304 (2012).
- [83] S. Goriely, *Nuclear Physics A* **933**, 68 (2015).
- [84] E. Chabanat, P. Bonche, P. Haensel, J. Meyer, and R. Schaeffer, *Nucl. Phys.* **A635**, 231 (1998).
- [85] J. Bartel, P. Quentin, M. Brack, C. Guet, and H.-B. Hakansson, *Nucl. Phys.* **A386**, 79 (1982).
- [86] J. F. Berger, M. Girod, and D. Gogny, *Nucl. Phys.* **A428**, 23c (1984).
- [87] M. Dutra, O. Lourenco, J. S. S. Martins, A. Delfino, J. R. Stone, and P. D. Stevenson, *Phys. Rev. C* **85**, 035201 (2012).
- [88] S. Goriely, N. Chamel, and J. M. Pearson, *Phys. Rev. C* **88**, 061302 (2013).